Department of Physics and Astronomy

Heidelberg University

Bachelor Thesis in Physics
submitted by

Britta Bader

born in Schwäbisch Hall (Germany)

September 2023

Absorption Imaging for Ultracold Gases of Dysprosium:

Optical Set-Up, Noise Analysis and Investigation of the Fitting Routine's Reliability

This Bachelor Thesis has been carried out by Britta Bader
at the Physikalisches Institut of the University of Heidelberg
under the supervision of Prof. Dr. Lauriane Chomaz.

Abstract

This thesis describes the design of an optical set-up for the performance of absorption imaging of an ultracold cloud of Dysprosium atoms. A telescope set-up made out of three lenses allows us to create a beam shape that accounts for the technical constraints originating from the experimental assembly. Furthermore, we investigate the main contributions to the noise occurring in the images taken with a CMOS camera. We find that non-illuminated images are dominated by read noise that is mostly statistically random, while illuminated images are instead dominated by fixed pattern noise mainly originating from a non-uniform illumination of the camera. We present a method to visibly reduce the latter. Finally, the reliability of the fit routine used in the experiment is investigated by applying it to simulated optical density images and comparing the results with the input values. In most cases condensate fraction and temperature are estimated well, while significant deviations remain for the estimation of the scattering length. We observe that the duration of the time of flight has no influence on the accuracy of the fit.

Kurzfassung

Die vorliegende Arbeit beschreibt den Entwurf eines optischen Aufbaus zur Abbildung eines Gases aus ultrakalten Dysprosium-Atomen mittels Absorptionsbildgebung. Ein Teleskop-Aufbau bestehend aus drei Linsen erzeugt einen Laserstrahl, dessen Form die Anforderungen, die durch den technischen Aufbau des Experiments gegeben sind, erfüllt. Des Weiteren wird untersucht, was die Hauptbeiträge zum Rauschen in den Bildern, welche mit einer CMOS-Kamera aufgenommen werden, liefert. Es wird beobachtet, dass in unbelichteten Bildern ”read noise” vorherrscht, welches statistisch zufällig auftritt, während in belichteten Bildern ”fixed pattern noise” dominiert. Es wird eine Methode aufgezeigt, mit der letzteres sichtbar reduziert werden kann. Zuletzt wird die Zuverlässigkeit der Fitroutine, die im Experiment zum Einsatz kommt, untersucht. Dabei wird diese auf simulierte ”optical density”-Bilder angewendet und das Ergebnis des Fits anschließend mit den Eingabewerten verglichen. In den meisten Fällen können der Anteil des Bose-Einstein-Kondensats an der gesamten Atomwolke sowie die Temperatur zuverlässig bestimmt werden. Lediglich bei der Streulänge kommt es zu größeren Abweichungen. Die Dauer des ”time of flight” hat keinen Einfluss auf die Genauigkeit des Fits.

Contents

Chapter 1

Introduction

1.1 Outline

> ”When you can measure what you are speaking about,
> and express it in numbers, you know something about it.”
> ∼ Lord Kelvin

Performing an experiment is pointless if you can not measure the result. Therefore, the imaging of the object that is under investigation is crucial for any experiment. In order to gain a reliable result one has not only to detect the object successfully but also be aware of the limits of the measurement.
This thesis presents an optical set-up that meets the constraints of the experimental apparatus to image an ultracold cloud of Dysprosium atoms using absorption imaging. Furthermore, possible noise sources of the set-up, which includes a CMOS camera, are investigated. With the results, the imaging process is simulated in a realistic way. This allows the examination of the reliability of the fitting procedure used in the experiment.
The present work was conducted in the group ”Quantum Fluids”, which operates under the leadership of Prof. Dr. Lauriane Chomaz at the Physikalisches Institute in Heidelberg. In the experiment a Bose-Einstein condensate is generated out of Dysprosium atoms. This element is particularly interesting because of its large magnetic moment which surpasses that of most elements in the periodic table. The goal of the experiment is the study of quantum phenomena of strongly interacting atoms in the two dimensional plane. While still being at a stage were the experiment is set up the creation of the first Bose-Einstein condensate just before this work started was a major milestone to achieve.

The following paragraph will provide a short overview of the content of this thesis. After giving short introductions to the experimental apparatus and to the absorption imaging technique, which may be helpful to follow the course of this thesis, we present the optical set-up for the performance of absorption imaging. First, we explain which factors influence the design. The beam’s shape is simulated to find the lens configuration that meets the requirements best. Afterwards, the chosen configuration is assembled in a test set-up and the shape of the beam undergoes a closer investigation to make sure it meets the requirements even if the lenses are slightly displaced. Furthermore, the beam polarisation is measured and a suitable set-up for imaging on a camera is put in place.

In the second part, we investigate the noise that is present in the set-up, which uses a CMOS camera. After explaining the operating principle of the camera and the noise classification that is used here, a so-called photon transfer curve is created. It represents a statistical approach to quantify the relevance of different types of noise in our imaging set-up. Subsequently, read noise, which dominates non-illuminated images, and fixed pattern noise, which dominates the illuminated ones, are under closer examination. We also introduce the flat fielding method which allows us to reduce the latter significantly.

After deriving the density profile of the atomic cloud in terms of experimentally accessible quantities, we can simulate the process of absorption imaging with the knowledge gained before. After applying the fit routine used on experimental data to simulated images, we compare the input parameters with the outcome. This allows us to make a statement on the reliability of the fit in different experimental settings.

1.2 Experimental Apparatus

The following section gives a short introduction to the assembly of the Dysprosium experiment. For more details please refer to [6], [7], [9] and [16]. A cross section through the experiment is shown in figure 1.1. In the present experiment a Bose-Einstein condensate (BEC) is created out of the bosonic Dysprosium (Dy) isotope Dy^{164}. The experimental set-up consists of two main parts: the 2D MOT chamber and the 3D MOT chamber, also called main chamber. MOT stands for magneto-optical trap. It is used to confine as well as to cool the atoms. The 2D MOT operates under high vacuum, the 3D MOT under ultra high vacuum. Both are connected via the so called differential pumping stage (DPS). The axis along this is referred to as the x-axis of the experiment while the one along gravity is the z-axis [9]. The Dy atoms evaporate from the oven as a hot atomic vapor jet into the 2D MOT chamber, where they are captured in the z, y-plane by magnetic gradients. These are formed by permanent magnets on the side of the chamber as well as four 421 nm laser beams. Here the atoms undergo a first cooling. From there a laser beam, the so called push-beam, which propagates along the x-axis, pushes them into the main chamber, where they are captured again in a 3D MOT. It is generated by two anti-Helmholtz coils that create a quadrupole field together with six 626 nm laser beams. Subsequently, they are loaded into an optical dipole trap (ODT), where they undergo evaporative cooling and finally condense into a BEC [6]. In the end, the lasers of the ODT are turned off and the atomic cloud expands freely for a time of flight before being imaged. The atomic cloud is supposed to be observed along the vertical as well as the horizontal axis. The imaging along the latter is the topic of this thesis. Due to a lack of space in other directions the imaging beam has to propagate along the x-axis of the experiment entering the experimental apparatus through viewport CF63 and exiting it through viewport CF40. This means it has to not only be superimposed with the push beam but also travel through all the experimental components before meeting the atomic cloud in the main chamber. Here the DPS presents a particular constraint due to its narrow diameter.

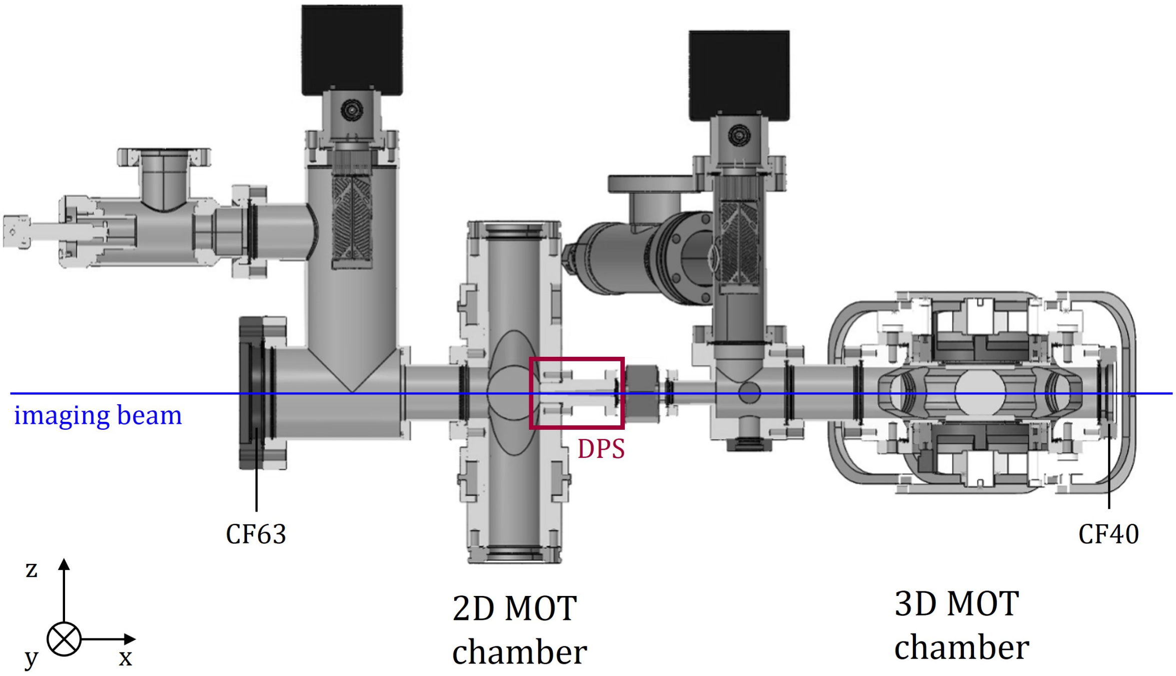

Figure 1.1: cross section through the assembly of the experiment in the x, z-plane; (blue) path of the imaging beam; (red) indication of the differential pumping stage (DPS) as main technical limitation to the shape of the beam

1.3 Absorption Imaging

At this point we want to give a short introduction to absorption imaging and describe how it is conducted in the present experiment. The following explanation is mainly adapted from [5]. Absorption imaging is a widely used technique for measuring the distribution of the atoms. It is performed by sending laser light of an appropriate wavelength through the atomic cloud to drive a transition from one atomic level to another. During this process the photon is absorbed by the atom. During spontaneous desexcitement photons are only emitted in random directions. Because of that, from the remaining light behind the cloud captured by a camera one obtains the inverse two dimensional density profile of the atomic cloud. In our case the ground level of the Dy atom is $[Xe]4f^{10}6s^2$ corresponding to a total angular momentum quantum number $J = 8$. The atom is excited from the $J = 8$ state to a $J' = 9$ state. The presence of a magnetic field leads to additional Zeeman-splitting between the m_J levels and the m'_J levels respectively. For temperatures we are interested in, we can assume that all atoms are in the $m_J = -8$ substate. As derived from the Glebsch-Gordan coefficients the transition to $J' = 9$, $m'_J = -9$ has a probability close to 1 [17]. In order to drive this transition a laser with wavelength $\lambda = 421$ nm with an intensity below $0.2\,\frac{\text{mW}}{\text{cm}^2}$ is sent along the x-axis of the experiment for a duration of $25\,\mu$s [9]. In the weak intensity regime, the reduction of the beam's intensity due to absorption by the atomic cloud with the density distribution $n(x, y, z)$ follows the law of Beer-Lambert.

The detected intensity in the y, z-plane is given by

$$I_{det}(y,z) = I_0(y,z) \exp\left(-\int \sigma_0 n(x,y,z)\,\mathrm{dx}\right) \tag{1.1}$$

where $I_0(y,z)$ denotes the incoming beam intensity and σ_0 refers to the absorption cross section. We assume that saturation effects do not play any role here. Using near resonant light allows use to express σ_0 as

$$\sigma_0 = \eta \frac{3\lambda^2}{2\pi} \qquad \text{with} \qquad \eta = \frac{1}{2} \quad . \tag{1.2}$$

The transition from the $m_J = -8$ substate to $m'_J = -9$ requires σ^- polarized light. However, in the experiment we use vertical linear polarized light, which can be decomposed in a σ^-- and a σ^+-component. This adds an additional factor $\eta = 1/2$ to the absorption cross section, since figuratively spoken only half of the light can be used to drive the transition. The transmission is defined as the ratio of detected and initial intensity.

$$T(y,z) = \frac{I_{det}(y,z)}{I_0(y,z)} = \exp\left(-\int \sigma_0 n(x,y,z)\,\mathrm{dx}\right) \tag{1.3}$$

Solving equation 1.3 leads to an expression for the column density.

$$n_{\mathrm{2D}}(y,z) = \int n(x,y,z)\,\mathrm{dx} = -\frac{1}{\sigma_0} \ln T(y,z) \tag{1.4}$$

In practice $T(y,z)$ is obtained by taking an image with the cloud, the so called absorption image $A(y,z)$, and dividing it by the background image $B(y,z)$, which is taken under the same conditions but without the atomic cloud. From both images an image without any incident laser light, the so called dark image $D(y,z)$, is subtracted in order to remove the background signal.

$$T(y,z) = \frac{A(y,z) - D(y,z)}{B(y,z) - D(y,z)} \tag{1.5}$$

In many cases the absorption is also characterized by looking at the optical density (OD) which is defined as

$$OD = -\ln T(y,z) = \int \sigma_0 n(x,y,z)\,\mathrm{dz} = \sigma_0 n_{2D}(y,z) \quad . \tag{1.6}$$

In our case the images are taken with a complementary metal oxide semiconductor (CMOS) camera, model Hamamatsu Orca Sparks. During one imaging run three images are taken in the following order: first the absorption image, than the background image and finally the dark image [9]. To this an appropriate density profile that includes the thermal cloud as well as the condensate is fitted. From this, one obtains the properties of the two components, such as size and atom number. With this information further quantities of the atomic cloud like condensate fraction, temperature and scattering length can be derived.

Chapter 2

Imaging Set-Up

2.1 Gaussian Beam

In this section, we review the relevant properties of the Gaussian beam that will be used in the remainder of this chapter. The following argumentation is adapted from [14].

The laser beam that is used for the imaging can be described in good approximation as a Gaussian beam. Characteristic of any Gaussian beam is that the intensity profile in the plane perpendicular to the axis of propagation follows a normal distribution. Assuming the beam propagates along the x-axis, than the intensity distribution in any y, z-plane follows a normal distribution and is only dependent on the radial distance r from the axis of the beam. The intensity distribution $I(r, x)$ is given by

$$I(r, x) = I_0(x) \exp\left(\frac{-2r^2}{w(x)^2}\right) \quad . \tag{2.1}$$

Here $I_0(x)$ denotes the intensity along the x-axis. In general $I_0(x)$ is not constant along the x-axis.

As indicator for the width of the beam the waist $w(x)$ is used. It is the radial distance from the x-axis to where the intensity has dropped to $1/e^2$ of the intensity in the center. The change of the beam waist along the x-axis is determined by a single parameter w_{min}, which is the minimal beam waist. Using the location of w_{min} as origin of the x-axis the beam waist along this axis follows a hyperbolic distribution.

$$w(x) = w_{min} \cdot \sqrt{1 + \left(\frac{x}{x_R}\right)^2} \tag{2.2}$$

The Rayleigh range x_R is given by

$$x_R = \frac{\pi w_{min}^2 n}{\lambda} \quad . \tag{2.3}$$

It describes the distance from the minimal waist to where the area of the cross section associated with this waist has doubled. Here λ denotes the wavelength of the laser light in vacuum and n the refractive index of the propagation medium. In our case it is assumed that $n = 1$ for the whole beam path. Since the size of the beam changes along the propagation axis, so does the maximum intensity $I_0(x)$. It is given by

$$I_0(x) = I_{max} \left(\frac{w_{min}}{w(x)} \right)^2 \quad . \tag{2.4}$$

I_{max} is the global maximal intensity, which is the intensity in the center of the beam at the location of the minimal waist. For distances $x \gg x_{min}$ far from the minimal waist equation 2.2 shows a linear dependence on x. Because of this, the half angle θ, which describes the divergence of the beam, can be calculated by

$$\theta = \lim_{x \to \infty} \arctan \left(\frac{w(x)}{x} \right) = \frac{\lambda}{\pi n w_{min}} \quad . \tag{2.5}$$

If a Gaussian beam is transmitted through a lens with focal length f, which can be treated as a thin lens, its wavefront changes. This affects size w'_{min} and location x'_{min} of the minimal waist after the lens in the following way

$$w'_{min} = M w_{min} \tag{2.6}$$

$$(x'_{min} - f) = M^2 (x_{min} - f) \tag{2.7}$$

with the magnification

$$M = \frac{M_r}{\sqrt{1 + r^2}} \tag{2.8}$$

where

$$r = \frac{x_R}{x_{min} - f} \qquad \text{and} \qquad M_r = \left| \frac{f}{x_{min} - f} \right| \quad . \tag{2.9}$$

In case the incident beam is collimated the Rayleigh range becomes infinitely large and x_{min} can be set to 0. As a result equations 2.6 and 2.7 reduce to

$$w'_{min} \approx \frac{\lambda}{\pi w_{min}} \cdot f \tag{2.10}$$

$$x'_{min} \approx f \quad . \tag{2.11}$$

The formulas presented here allow us to calculate the beam's shape formed under the influence of some lenses. What the shape of the beam is supposed to look like in order to propagate undisturbed through the experimental apparatus and which other requirements it has to meet will be presented in the next section.

2.2 Requirements and Technical Constraints

The imaging is conducted along the x-axis of the experiment as defined in 1.1. This means that the laser beam goes through viewport CF63 into the 2D MOT chamber and than through the DPS to the main chamber where the absorption takes place. This leads to some constraints on the shape of the beam, which will be presented in the following.

When it comes to the size of the beam the main restriction originates from the DPS. The DPS has an initial radius of only 1 mm, which becomes larger with a half angle of $\alpha_{\text{DPS}} = 2°$ over a length of 55.7 mm [7]. The goal is to create a beam that is small enough to prevent any relevant cut-off due to the DPS.

A second constraint comes from the object to be imaged. The atomic cloud is positioned in the centre of the 3D MOT chamber, which has a distance of 328 mm in reference to the DPS, as can be seen in figure 1.1. We want to image three different situations. First of all, we want to examine the atomic cloud during the loading of the 3D MOT. At this point the cloud has a size of about 1 mm after a short time of flight of about 5 ms. A magnification of 0.5 is used for imaging on the camera. The vertical displacement of the cloud in negative z-direction s_z due to gravity after switching off the trap is given by

$$s_z = \frac{g}{2} t_{tof}^2 \tag{2.12}$$

with g denoting the gravitational acceleration. For a time of flight duration of 5 ms, we obtain $s_z = 0.12\,\text{mm}$. Secondly, we are interested in the atomic cloud after compression with a time of flight of about 12 ms, which leads to a vertical displacement of 0.71 mm. The atomic cloud has a size of roughly $1\,\text{mm} \times 200\,\mu\text{m}$ and usually a magnification of 2 is used. Finally, we want to image the BEC after a long time of flight, which typically takes about 20 ms. This corresponds to a vertical displacement of $s_z = 1.96$ mm, while the atomic cloud itself reaches a size of $30 \times 60\,\mu\text{m}$. The camera that is used in the set-up has a sensor size of about $7.03 \times 11.25\,\text{mm}$. Using a magnification of 2 (more on this in section 2.7) leads to an effective sensor size of 3.52 mm in vertical direction and using a magnification of 0.5 to an effective sensor size of about 14 mm. For the sensor being fully illuminated in vertical direction, we aim for a beam waist of 9 mm in the position of the atomic cloud.

That means our goal is a beam that is small enough in the area around the DPS to prevent any cut-off and at the same time large enough in the plane of the atomic cloud to picture the atomic cloud with an adequate intensity. In order to achieve this the minimal waist is supposed to be located within the DPS. When looking at a cross section of the DPS in the x, z-plane the minimal waist x_{min} has its optimal position at the intersection of the diagonals from the corners of the DPS as shown in figure 2.1. With this the half angle of the divergence of the beam ϑ can be up to

$$\vartheta = \tan\left(\frac{2.9\,\text{mm} + 1\,\text{mm}}{55.7\,\text{mm}}\right) \approx 4° \tag{2.13}$$

before the beam is cut by the DPS.

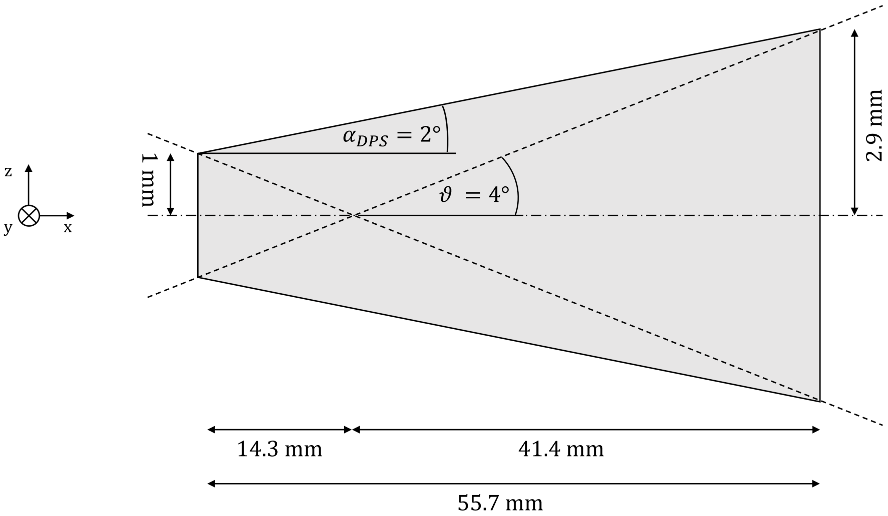

Figure 2.1: sketch of the DPS

Since the whole experiment is performed under high and ultra high vacuum, all the optical apparatus have to be set up in front of viewport CF63, which has a window with a radius of roughly 30 mm. Furthermore, the 626 nm push beam, which transfers the atoms from the 2D MOT chamber to the 3D MOT chamber, goes along the same axis as the imaging beam. Therefore, both laser beams are superimposed using a polarizing beam splitter (PBS) just in front of the viewport. The imaging beam is reflected at the PBS, while the push beam is transmitted. However, this requires the last lens of the optical set up to keep a distance from the viewport of at least about 100 mm in order to leave enough space for that. This means the distance of the last lens to the optimal position of the minimal waist is supposed to be at least 370.3 mm.

The beam exits the 3D MOT chamber via viewport CF40, which is located at a distance of about 414 mm from the minimal waist. At this position the waist should not exceed the radius of the viewport of roughly 20 mm. The camera is placed behind that. Finally, the use of mainly two inch optics requires the waist of the beam to be smaller than 2.56 mm at any optical component. Due to limited space on the breadboard where the set-up is supposed to be mounted the optical path should not be too long.

To conclude, tabel 2.1 provides an overview of the constraints to the beam size at different positions.

	last lens	CF63	DPS beg	DPS end	atomic cloud	CF40
position x [mm]	< -100	0	206	261.7	534	635
waist $w(x)$ [mm]	< 25.4	< 30	< 1	< 2.9	> 9	< 20

Table 2.1: constraints on the size of the beam waist imposed by the assembly of the experiment; positions are given relative to viewport CF63

2.3 Simulation and Design of the Optical Set-Up

To find the optical set-up that fulfills the requirements best, the size of the beam at the relevant positions is simulated for a telescope set-up with three lenses. The calculations on which this is based are presented below. For more details about the actual program please refer to appendix A.2.

As input parameters the simulation takes the focal lengths of the lenses f_1, f_2 and f_3, as well as their absolute distances l_1, l_2 and l_3 from viewport CF63. The numbering follows the order in which the lenses are penetrated by the beam.

The light exits a single mode fibre with an effective numerical aperture of $NA_{e^2} = n \cdot \theta = 0.068$. After that a lens with focal length $f_0 = 15\,\text{mm}$ is used to create a collimated beam with a waist of $w_0 = 1.022$ mm. The first lens is a 1” lens. The influence it has on size w_1 and position x_1 of the minimal waist after the lens can be approximated by equation 2.10 and 2.11.

$$w_1 \approx \frac{\lambda}{\pi w_0} \cdot f_1 \qquad x_1 \approx f_1 \tag{2.14}$$

The position of the minimal waist x_1 in reference to the second lens is given by

$$\tilde{x}_1 = l_1 - l_2 - x_1 \quad . \tag{2.15}$$

With this we calculate the impact of lens 2 on the waist according to equation 2.6 and 2.7 as

$$w_2 = M w_1 \qquad (x_2 - f_2) = M^2(\tilde{x}_1 - f_2) \quad . \tag{2.16}$$

In reference to the third lens the position of the minimal waist is given by

$$\tilde{x}_2 = l_2 - l_3 - x_2 \quad . \tag{2.17}$$

With this we obtain size w_3 and position x_3 of the minimal waist after lens 3 from

$$w_3 = M w_2 \qquad (x_3 - f_3) = M^2(\tilde{x}_2 - f_3) \quad . \tag{2.18}$$

The position of the minimal waist in reference to viewport CF63 is

$$\tilde{x}_3 = x_3 - l_3 \quad . \tag{2.19}$$

Size w_3 and position $\tilde{x}_3$ of the minimal waist after lens 3 determine the shape of the beam as it propagates through the experiment. With this information we can determine the waist at the relevant positions x listed in table 2.1 from equation 2.2.

$$w(x) = w_3 \cdot \sqrt{1 + \left(\frac{x - \tilde{x}_3}{x_R}\right)^2} \qquad \text{with} \quad x_R = \frac{\pi w_3^2}{\lambda} \tag{2.20}$$

As input to the simulation, we use the focal lengths of the lenses that are available in the laboratory. The positions of the lenses are changed in step sizes of 5 mm. To the outcome we apply the constraints listed in table 2.1. Some possible configurations are presented in table 2.2. The values for the distances l_1, l_2, l_3 and beam waists w(DPS beg), w(DPS end), w(BEC) correspond to the mean values we obtain when taking the results for different lens positions that still fulfill the requirements. The parameters d_{12} and d_{23} denote the distances between the focal point of lens 1 to the position of lens 2 and the focal point of lens 2 to the position of lens 3 respectively. The minimum and maximum values given in the table can be used as an indication of how much the lenses can be displaced with respect to each other and still create a beam that fulfills the requirements. All the possible configurations create very similar beam waists around the DPS and in the plane of the atomic cloud. Of the lenses we have in stock there is no option but to use a lens with a focal length ±60 as first lens. Using a negative focal length can shorten the overall path by several centimeters. In the case of two lenses with focal length $f_2 = f_3 = 100$, the minimum and maximum values of d_{12} and d_{23} only differ by 20 mm. This means that the set-up of the lenses would have to be very precise to still fulfill the requirements to the beam shape. Because of that, this option is excluded. With the third lens being $f_3 = 250$ we have four different options for the middle lens. In the end we choose the one with the largest focal length, since it provides the shortest mean overall optical path and the possible displacement of the lenses is the largest.

f_1	f_2	f_3	l_1	l_2	l_3	d_{12}	d_{23}	w(DPSbeg)	w(DPSend)	w(BEC)
-60	100	100	902	385	121	515-635	135-145	0.33	1.59	10.96
	250	250	970	960	126	60-95	860-1000	0.31	1.53	10.56
	300		960	939	127	60-120	830-1020	0.32	1.54	10.64
	500		946	861	125	60-255	775-1195	0.32	1.54	10.65
	750		921	751	121	60-380	755-1195	0.32	1.57	10.82
60	100	100	974	374	106	515-565	145-145	0.32	1.56	10.72
		250	972	907	159	0-10	715-790	0.31	1.50	10.33
	250	250	975	900	157	0-35	715-795	0.31	1.50	10.34
	300		976	896	157	0-45	715-795	0.31	1.50	10.32
	500		978	881	156	0-85	715-810	0.31	1.50	10.34
	750		981	779	141	0-380	715-1195	0.31	1.49	10.27

Table 2.2: possible configurations for a telescope set-up with three lenses of focal lengths f_1, f_2 and f_3; the values for the distance of the lenses l_1, l_2 and l_3 from viewport CF63 and the waist of the beams at the beginning w(DOS beg) and end w(DPS end) of the DPS as well as in the plane of the atomic cloud w(BEC) are the mean values for those lens positions that fulfill the requirements; the distances between focal point and following lens d_{12} and d_{23} are minimum and maximum values; all values are given in mm

To summarize, in the end, we chose a telescope set-up with three lenses, the first one being a 1” lens with a negative focal length of $f_1 = -60$ mm, followed by two 2” lenses with the focal lengths $f_2 = 750$ mm and $f_3 = 250$ mm. The first one is placed at a distance from viewport CF63 of roughly $l_1 = 830$ mm; the others are at $l_2 = 730$ mm and $l_3 = 150$ mm. How the beam is expected to propagate for the chosen configuration is displayed in figure 2.2. The minimal waist is expected to be $w_{min} = 4.687\,\mu$m.

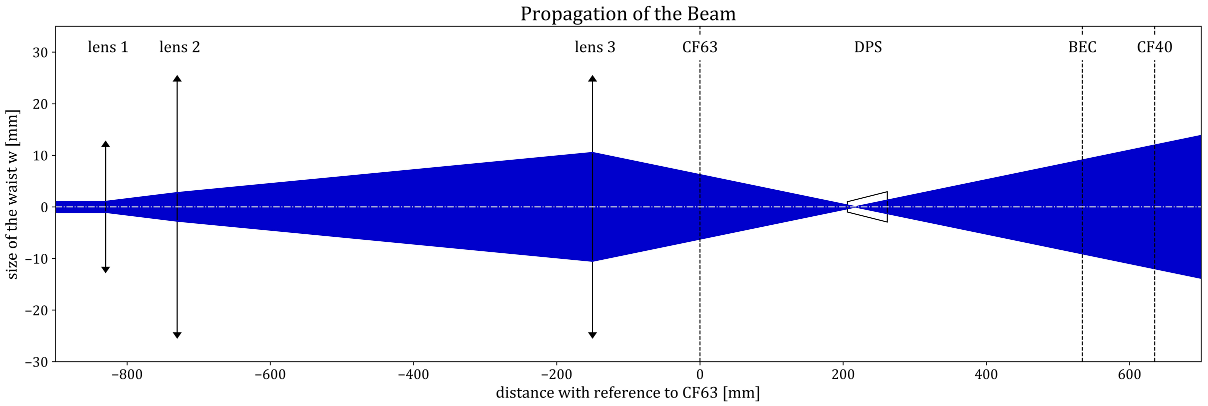

Figure 2.2: calculated shape of the beam (blue) as indicated by the waist when propagating through the optical set-up and the experiment

Now we want to know, if the beam created by the chosen configuration is expected to be cut by any optical apparatus. As a first indicator, the radius of the beam is defined as three times the waist. At this distance from the propagation axis the intensity of the beam has fallen to 0.03 % compared to the center and any cut-off beyond this is considered as neglectable. If the size of the beam extends that of any component, the size that the beam gets due to the physical boundary is considered as the radius.

An overview of the expected waists and radii at positions of interest is given in table 2.3. With a radius of $r_0 = 3.066$ mm the collimated beam is clearly smaller than the radius of a 1” lens. At the position of the second lens the radius is $r_2 = 8.16$ mm and does also not extend the size of the 2” lens. A cut-off occurs only at lens 3. At this point the size of the beam is reduced from 31.491 mm to the size of the 2” lens. Because of this, there is no further cut-off by any of the viewports nor the DPS.

	lens 1	lens 2	lens 3	CF63	DPS beg	DPS end	BEC	CF40	camera
waist [mm]	1.022	2.725	10.497	6.209	0.320	1.273	9.058	11.945	21.923
radius [mm]	3.066	8.176	25.4	7.042	0.362	1.444	10.272	13.547	24.863

Table 2.3: theoretical expectations of the size of the beam at relevant positions in the experiment, after lens 3 the radius is determined by the cut-off at lens 3

In the experiment the whole optical set-up is supposed to be mounted on a 325 × 650 mm breadboard while still leaving enough space for the set-up of the push-beam. A scale drawing of the spacial arrangement is shown in figure 2.3.

The imaging beam and the push beam are superimposed at a 1” PBS. When hitting the PBS the beam has a radius of 10.2 mm, which is about the size of the PBS. As confirmed in a test set-up, this does not affect the functionality of the set-up any further. However, this is not included in the simulation.

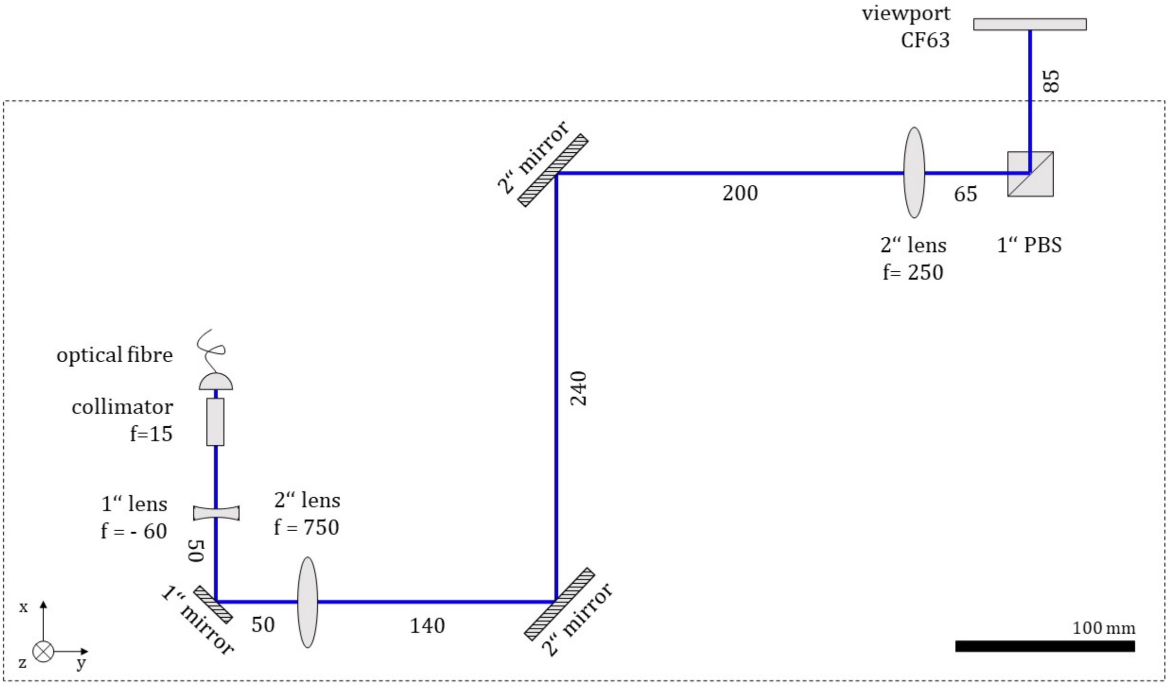

Figure 2.3: spacial arrangement of the optical set-up on the breadboard as scale drawing

Furthermore, we are interested in the intensity with which the cloud is expected to be imaged. From equation 2.1 the intensity at the outer edge of the beam compared to the center can be calculated as

$$\frac{I(r = r_{\mathrm{BEC}}, x = 534\,\mathrm{mm})}{I(r = 0, x = 534\,\mathrm{mm})} = \exp\left(-2\frac{r_{\mathrm{BEC}}^2}{w_{\mathrm{BEC}}^2}\right) \quad . \tag{2.21}$$

In the plane of the atomic cloud, i.e. at a position $x = 534\,\mathrm{mm}$, the beam has a waist of $w_{\mathrm{BEC}} = 9.058$ mm and a radius of $r_{\mathrm{BEC}} = 13.547\,\mathrm{mm}$. With this, we obtain an intensity at the outer edge of the beam of 7.6 % compared to the center. It is also relevant to know the intensity at the edge of what can still be imaged. Assuming a magnification of 2, we are interested in a position 7.03 mm in z-direction and 11.25 mm in y-direction from the center. Here the intensity is still 30 % and 5 % respectively.

2.4 Measurement of the Beam Waist

How large the beam along its propagation axis is in practice is measured in a test set-up. We use two different measuring techniques depending on the size of the beam.

At positions around the minimal waist the measurement is done directly by using a camera, which records a two dimensional picture of the intensity profile of the beam at the position of its sensor. The sensor consists of 1624 × 1224 pixels with a size of 4.4 × 4.4 μm each. With this an area up to 7.1 × 5.3 mm can be imaged [13]. Therefore, we can measure beam waists up to 2.64 mm with this camera. Since the minimal waist is only about the size of one pixel, it can not be measured directly. Experimentally, we find that the beam has to be larger than about 100 μm to obtain a reliable result. In accordance with equation 2.1 the waist at each measurement position is determined from fitting a two dimensional Gaussian distribution to the beam profil

$$G(y,z) = A \cdot \exp\left(-\frac{(y-\mu_y)^2}{2\sigma_y^2} - \frac{(z-\mu_z)^2}{2\sigma_z^2}\right) + C \tag{2.22}$$

with A as amplitude and C as offset. The center in y (z) direction is given by μ_y (μ_z) and the standard deviation by σ_y (σ_z). Comparing 2.22 and 2.1 reveals that the waist corresponds to two times the standard deviation. The cross section of the beam is approximately circular. Thus, the mean of the σ-values from both directions is taken in order to obtain the effective waist. The error of the waist Δw is given by the sum in quadrature of the errors of the corresponding fit parameters $\Delta\sigma_y$ and $\Delta\sigma_z$.

$$w = \frac{1}{2}(2 \cdot \sigma_y + 2 \cdot \sigma_z) \qquad \Delta w = \sqrt{(\Delta\sigma_y)^2 + (\Delta\sigma_z)^2} \tag{2.23}$$

An example for obtaining the waist from the image recorded with the method described above is shown in figure 2.4.

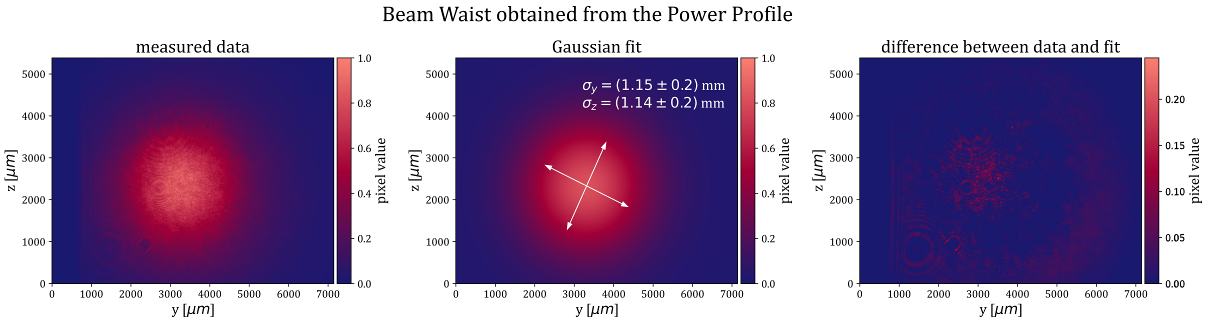

Figure 2.4: (left) intensity profile of the beam at a distance of about 140 mm after viewport CF63, (middle) Gaussian fit used to determine the beam waist, (right) fit residue

Further away from the minimal waist the size of the beam extends the size of the sensor. In this case, we employ another technique. A pupil with 1 mm diameter is used in order to shield everything but a small portion of the beam. It is placed in front of a powermeter, which measures the power going through the pupil. Therefore, it provides a local estimate of the intensity at the position of the pupil. We perform a beam waist measurement by shifting the pupil in steps of 1 mm along the y-axis, i.e. perpendicularly to the beam propagation. The result corresponds to a cross section through the power profile of the beam along the y-axis. To the measured values a one dimensional Gaussian fit is applied

$$G(y) = A \cdot \exp\left(-\frac{(y-\mu)^2}{2\sigma^2}\right) + C \tag{2.24}$$

were A and C again denote amplitude and offset. The center is indicated by μ and the standard deviation by σ. Comparing equation 2.24 to 2.1 again reveals that the beam waist is obtained by multiplying the standard deviation by two. Since equation 2.1 is separable in y and z direction a displacement from the center in one direction does not effect the size of the waist in the other.

This allows the measurement to be still reliable even if the pupil is not centered on the z-axis. Two examples where the waist of a larger beam is determined are presented in figure 2.5.

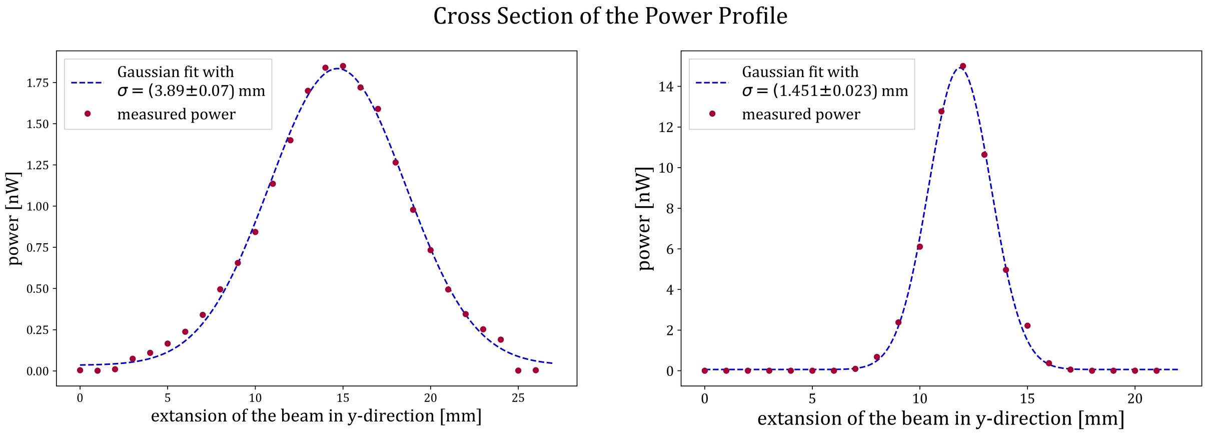

Figure 2.5: measurement of the power going through a pupil with ∅ 1 mm as a function of its position in y-direction for a beam at about 60 mm in front of viewport CF63 (left) and 110 mm behind (right)

At this point we have obtained the beam sizes as indicated by the waist for different positions along the x-axis. Since the absolute position in reference to other optical components is determined by hand with a ruler, there is a systematic error for each set of measurements. In order to avoid that the data points from both methods are shifted against each other the position of the minimal waist is first determined for each set individually by applying formula 2.2 and than adjusted to the theoretically expected position. After that the same formula is fitted to all values. The results are shown in figure 2.6.

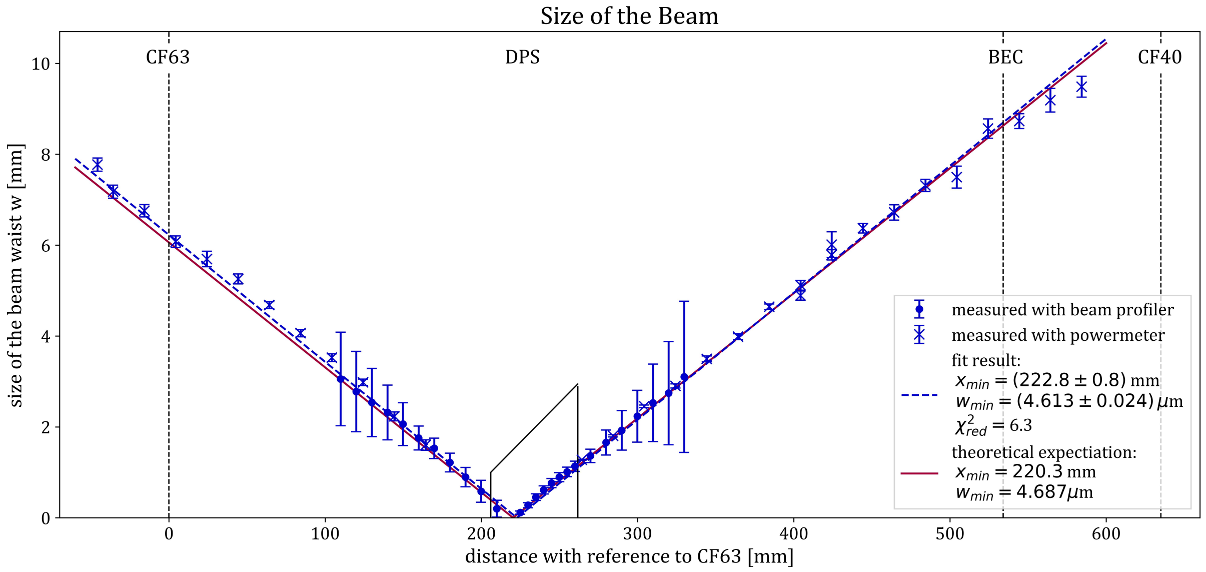

Figure 2.6: measured beam waist as function of the distance along the x-direction obtained with a beam profiler (dots) and a powermeter (crosses), to this the function $w(x) = w_{min} \cdot \sqrt{1 + (x/x_R)^2}$ is fitted (blue); theoretical expectation (red) for comparison; positions of relevant components are indicated as reference

From the fit one obtains a minimal waist of $w_{min} = (4.613 \pm 0.024)\,\mu\text{m}$ compared to an expected value of $w_{min} = 4.687\,\mu\text{m}$. This corresponds to a deviation of about 3σ, which means that the experimental results suit the expectations well. This is especially surprising, since we would not have expected to achieve such a high focus with the type of lenses that are used in the present set-up.

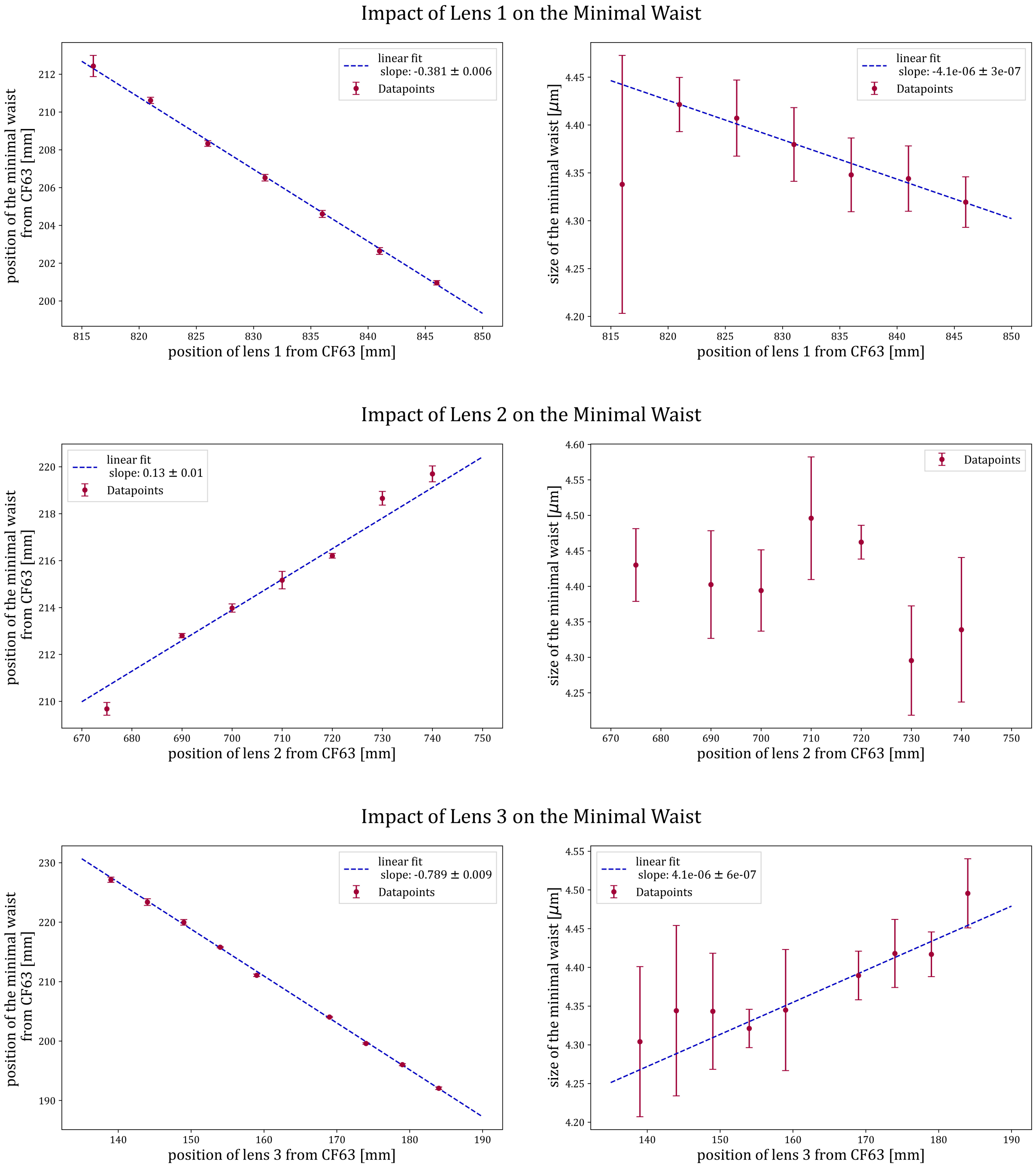

Figure 2.7: effects on position (left) and size (right) of the minimal waist when changing the position of lens 1 (top), 2 (middle) or 3 (bottom) individually

2.5 Effects of Lens Displacement

In a test set-up we investigate how size and position of the minimal waist change with the displacement of one of the three lenses. For each of the three lenses its position is changed while the position of the other two is kept constant. Since the minimal waist is too small to be measured directly, for each position of the lens the intensity distribution of the beam profile is measured at different distances around the minimal waist with a beam profiler and the waist is extracted as described above. The minimal waist is now extracted by fitting equation 2.2 to all the obtained values. With this, one has the size and position of the minimal waist for each position of one lens. How these values change with the position of the three lenses is shown in figure 2.7.

The displacement of lens 3 has the strongest impact on the minimal waist. Moving the lens by 1 mm shifts the minimal beam waist by (0.789 ± 0.009) mm. A displacement by 10 mm causes the size of the minimal waist to change by (41 ± 6) nm. The further away from the viewport lens 3 is placed, the closer is the position of the minimal waist and the larger it becomes.

Looking at the first lens it is observed that a displacement by 1 mm causes the minimal waist to move by (0.381 ± 0.006) mm into the same direction. The impact on the size of the minimal waist is about the same as for lens 1, namely (41 ± 3) nm for a displacement of 10 mm. Moving the lens away from the viewport leads to larger minimal waist.

The effect of lens 2 is smaller than that of the other lenses. Moving this lens 1 mm further away from the viewport makes the minimal waist shift by only (0.13 ± 0.01) mm. The impact on the size of the minimal waist is so small that it can not be resolved.

To draw a conclusion we can say that moving lens 3 is best suited to change the shape of the beam significantly, since it influences the position and size of the waist equally. Changing the position of the first lens has less impact on the position of the waist and therefore may be used if one wants to mainly influence the degree of divergence. The middle lens can help when doing the fine-tuning of the set-up and setting the position of the minimum waist precisely.

2.6 Beam Polarisation

For the absorption process we plan to use light that is as linear polarized as possible. To look at the pureness of the polarisation after the PBS a half wave plate is placed in front of another PBS. The orientation of the wave plate is rotated and the maximum and minimum power after the second PBS are recorded with a powermeter. The following values are measured.

$$\begin{aligned} &\text{maximum} \qquad P_{max} = (375 \pm 1)\,\mu W \\ &\text{minimum} \qquad P_{min} = (1.90 \pm 0.05)\,\mu W \end{aligned}$$

This corresponds to a degree of polarization of 99.5%, which is a satisfying result. However, one has to note, that this measurement is not very precise since the PBS used for the measurement itself has an extinction ratio of only 1000:1 according to the manufacturer.

2.7 Image Projection Set-Up

To measure the atomic density distribution, the plane of the atomic cloud has to be imaged onto the plane of the camera. This is achieved by using an imaging lens. The distance from lens to object a and the distance from lens to camera b has to fulfill the following relation with the focal length f of the imaging lens.

$$\frac{1}{a} + \frac{1}{b} = \frac{1}{f} \tag{2.25}$$

The magnification M is given by

$$M = \frac{a}{b} \quad . \tag{2.26}$$

In the experiment one wants to image the atomic cloud at three different stages of the cooling process as described in section 2.2. Depending on the case a lens with focal length $f = 100$ mm is placed at either one of two positions behind the viewport CF40. For imaging the atomic cloud during the loading of the 3D MOT, the lens is placed $a = 300\,\text{mm}$ behind the atomic cloud and $b = 150\,\text{mm}$ in front of the camera, while for imaging the compressed cloud it is the other way around. An overview of both lens positions is shown in figure 2.8. The set-up was tested with a razors blade as object. After setting the camera and one of the lenses roughly at the right positions in reference to the object, they are aligned by hand, so that the image is as clear as possible. After that the lenses are exchanged. After slightly changing the camera position, the alignment is repeated for the first lens.

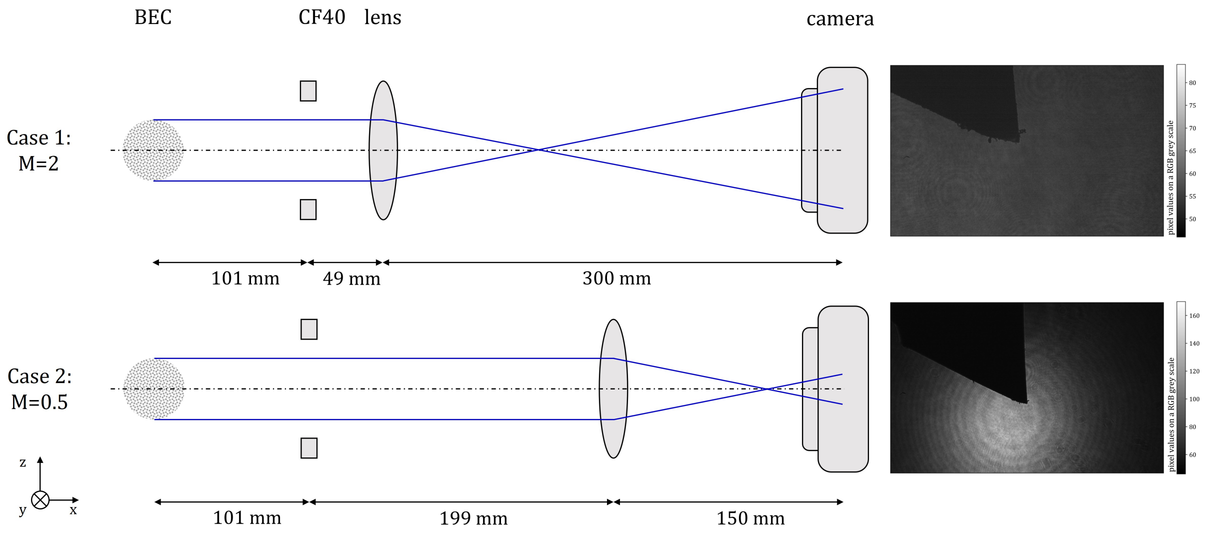

Figure 2.8: illustration of the imaging with a magnification of $M = 2$ (top) and $M = 0.5$ (bottom)

To estimate the maximum time of flight t_{tof} that can be used imaging the BEC with different magnifications the following calculation is done. The camera sensor has a size of 7.03×11.25 mm. With a magnification of $M = 2$ this corresponds to an effective pixel size in the vertical of about 3.5 mm and with a magnification of $M = 0.5$ to an effective pixel size of about 14 mm. Initially, the cloud is in line with the center of the sensor. Therefore, the maximum movement in vertical direction due to gravity corresponds to half the effective size. With

$$t_{tof} = \sqrt{\frac{2s_z}{g}} \tag{2.27}$$

we obtain a maximum time of flight of 19 ms for $M = 2$ and 38 ms for $M = 0.5$.

Chapter 3

Noise Analysis

3.1 Operating Principle of the Camera

In the imaging set-up we use the camera model ORCA spark manufactured by Hamamatsu. The following paragraph follows the description provided in the manual [11]. The camera operates with a CMOS sensor, short for Complementary Metal Oxide Semiconductor. Figure 3.1 shows the schematic construction of the sensor chip. When light enters a pixel the photons are converted into charge by a photodiode. The probability that a photon triggers an electron is given by the quantum efficiency (QE). At a wavelength of 421 nm the sensor's QE is about 70 %. Different from a charge-coupled device (CCD) sensor the charge is directly converted into voltage in every single pixel by an amplifier. Every pixel has a switch to output its voltage. Every horizontal line is then converted into a digital signal by an analog-to-digital converter (ADC). In order to reduce the noise the sensor has a correlated double sampling circuit (CDS) on the chip that removes a potential off-set.

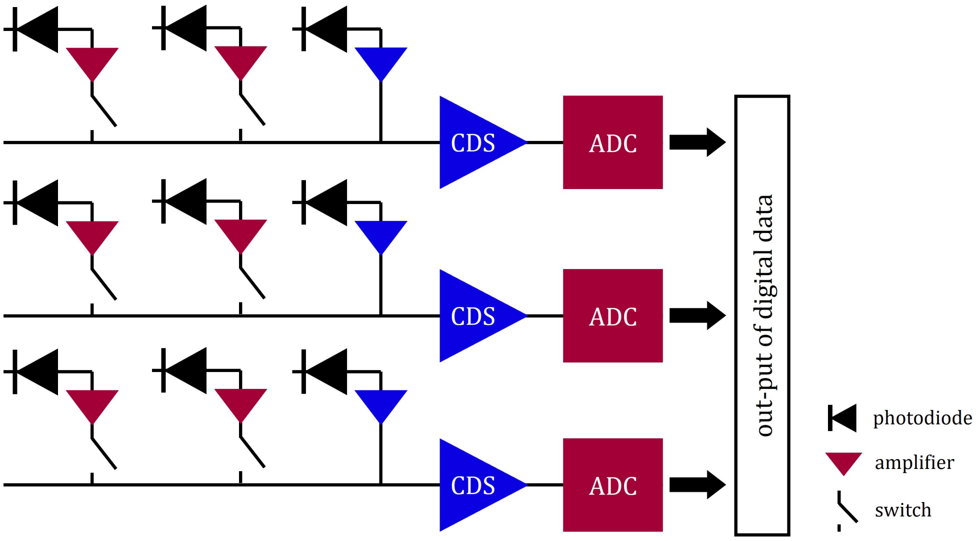

Figure 3.1: schematic representation on the construction of a CMOS camera sensor: for each pixel the incident photons are converted into charge in a photodiode and than converted into voltage by an amplifier, each horizontal line has its own ADC to out-put a digital signal and CDS to reduce noise; adapted from [11]

In the next sections we will examine in which way the sensor, among other things, contributes to the noise that occurs during the imaging process. After giving an overview over potential noise sources, we look at the photon transfer curve to identify the relevant ones. Additionally, we examine the read noise and the fixed pattern noise in more detail and try to reduce the latter by image processing.

3.2 Noise Classification

The following section presents an overview of potential noise sources during imaging and their classification. We differentiate four types of noise by their impact on the statistical behaviour of the signal: read noise, photon shot noise (PSN), fixed pattern noise (FPN) and the full-well noise. Several physical sources can contribute to each type of noise [8].

Read noise refers to any noise that is independent of the signal. It occurs even without the incoming of any light. It adds an off-set to the variance of the signal independent of the mean signal.

$$\sigma^2_{\text{read}} = const \tag{3.1}$$

Photon shot noise (PSN), which is quantified by the standard deviation σ_{PSN} from the mean signal, has its origin in the quantized nature of light [5]. For common light sources the incoming number of photons follows a Poisson statistic [4]. Since the quantum efficiency is independent of the number of photons received for a certain wavelength, σ_{PSN} can be expressed as

$$\sigma_{\text{PSN},e^-} = \sqrt{\bar{N}_{e^-}} \tag{3.2}$$

were $\bar{N}_{e^-}$ denotes the average number of generated photo electrons [8]. To express this in terms of the digital signal, one introduces the translation factor $F(e^-/\text{counts})$, which tells how many electrons correspond to one digital count assuming a linear dependency [8]. Therefore, a signal and its noise translate according to

$$N_{e^-} = F(e^-/\text{counts}) \cdot N_{\text{count}} \qquad \text{and} \qquad \sigma_{e^-} = F(e^-/\text{counts}) \cdot \sigma_{\text{count}} \quad . \tag{3.3}$$

Inserting these relations into equation 3.2 provides us with an expression for PSN in terms of digital units.

$$\sigma_{\text{PSN}} := \sigma_{\text{PSN, count}} = \sqrt{\frac{\bar{N}_{\text{count}}}{F(e^-/\text{counts})}} \tag{3.4}$$

Therefore, the variance σ^2_{PSN} scales linear with the number of mean counts.

$$\sigma^2_{\text{PSN}} \propto \bar{N}_{\text{counts}} \tag{3.5}$$

Fixed pattern noise (FPN) quantified by the standard deviation σ_{FPN} refers to any spatial differences in the number of counts that do not change over time. It might be either caused by photo response non-uniformity (PRNU), which describes a difference in sensitivity that is individual to each pixel due to slight variations in the manufacturing [12], or a time constant non-uniform illumination of the sensor [8]. We define the so called FPN quality factor Q_{FPN} that defines over which range the signal spreads due to FPN [8]. With this σ_{FPN} is defined as

$$\sigma_{\mathrm{FPN}} = Q_{\mathrm{FPN}} \cdot \bar{N}_{\mathrm{counts}} \quad . \tag{3.6}$$

FPN contributes to the quadratic term of the variance [8].

$$\sigma^2_{\mathrm{FPN}} \propto \bar{N}^2_{\mathrm{counts}} \tag{3.7}$$

The last type of noise, the full-well noise quantified by the standard deviation $\sigma_{\text{full-well}}$, exhibits some irregular, non-linear and non-quadratic dependency. Often the variance decreases with increasing mean count. This is caused by the pixels one by one becoming saturated, the so called full-well [8].

All noise sources are considered as independent from each other and therefore add in quadrature to a total variance of

$$\begin{aligned} \sigma^2_{\mathrm{tot}} &= \sigma^2_{\mathrm{read}} + \sigma^2_{\mathrm{PSN}} + \sigma^2_{\mathrm{FPN}} + \sigma^2_{\text{full-well}} && (3.8) \\ &= \sigma^2_{\mathrm{read}} + \frac{1}{F(e^-/\mathrm{counts})} N_{\mathrm{counts}} + (Q_{\mathrm{FPN}} N_{\mathrm{counts}})^2 + \sigma^2_{\text{full-well}} \quad . && (3.9) \end{aligned}$$

To determine the relevant types of noise in the present set-up, we use a statistical approach by calculating the so-called photon transfer curve (PTC).

3.3 Photon Transfer Curve

The PTC refers to a graph whereby the variance of the signal is plotted over its mean and allows us to compare the different noise contributions. The procedure, how we record the PTC, mainly follows the description provided in [8]. The PTC is recorded in the unit of digital counts. To vary the mean count either the light intensity or the exposure time of the sensor, i.e. the duration of the imaging pulse, is changed. In our case it is the latter. We use laser pulses with ten different durations between 5 and 140 μs and perform ten repetitions each. We do not look at the sensor as a whole but at a subarray of a certain size. From a statistical point of view one wants as many data points as possible, i.e. as many pixels as possible, since the accuracy scales with the square root of the number of pixels [8]. On the other hand, if the area is too large the influence of effects like nonuniform illumination becomes too dominant. After testing different sizes, we choose an area of 10×10 pixels, which corresponds to a number of pixels of $N_{px} = 100$. The area is centered where the atomic cloud used to be imaged.

First, the mean values i.e. the values on the horizontal axis are determined. For this we subtract from each image pixel by pixel the dark image, which is taken under the same conditions but without any laser light. With this we eliminate the offset signal that is added to each image independent of the incident light. However, the noise that goes along with the dark signal does still contribute to the variance. After the subtraction we calculate the average signal $\bar{N}_{\text{count}}$ for the subarray. The whole process can be described in terms of a formula by

$$\bar{N}_{\text{count}} = \frac{\sum_{i=1}^{N_{px}} N_{\text{count},i} - N_{\text{count, dark, i}}}{N_{px}} \tag{3.10}$$

where $N_{\text{count},i}$ denotes the digital count of each pixel of the illuminated image and $N_{\text{count, dark, i}}$ that of the dark image.
Secondly, the variance values used for the vertical axis are obtained. This is done by calculating the variance of the pixel values $\sigma^2_{N_{\text{count}}}$ after removing the dark image.

$$\sigma^2_{N_{\text{count}}} = \frac{\sum_{i=1}^{N_{px}} \left((N_{\text{count},i} - N_{\text{count, dark, i}}) - \bar{N}_{\text{count}}\right)^2}{N_{px}} \tag{3.11}$$

We calculate mean count and variance of each pulse duration for each of the 10 repetitions and then take the average. The error on the obtained values correspond to the standard deviation from the averaging. The resulting PTC is presented in figure 3.2.

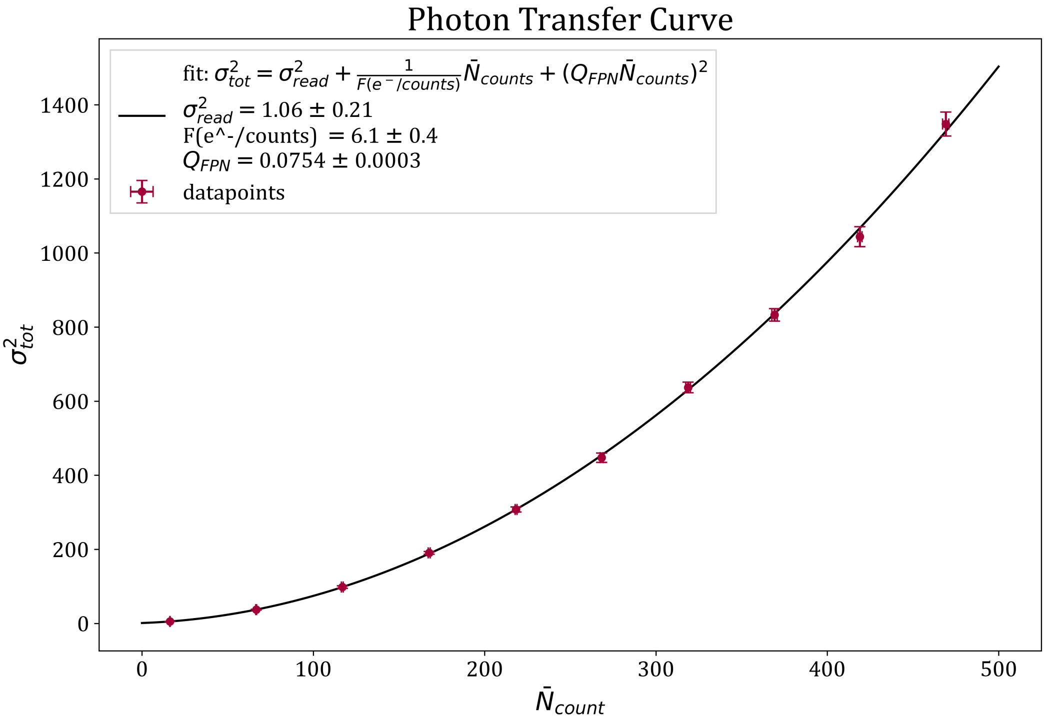

Figure 3.2: PTC for imaging with laser light of a wavelength of 421 nm; the data points (red) give the mean and the variance of digital counts over 100 pixels, the errorbars correspond to the standard error from 10 repetitions, to this a second order polynomial fit (black) is applied; see text for details

Because of equation 3.9 a second order polynomial fit is applied to the data points. From this we obtain a translation factor of $F(e^-/\text{counts}) = 6.1 \pm 0.4$, which means that the creation of about six electrons results in one digital count. For the FPN quality factor we get $Q_{\text{FPN}} = 0.0754 \pm 0.0003$. According to [8] the FPN quality factor would normally be in the order of 0.01, if it originated only from PRNU. This indicates that non-uniform illumination that is constant over time has an effect here.

If one looks at the PTC in double logarithmic scale as presented in figure 3.3 different regimes can be distinguished easily. In theory, the PTC exhibits four regimes each corresponding to the dominance of a different type of noise. The read noise leads to a constant off-set on the PTC [8] and dominates the total variance for low signals. It is followed by the PSN regime, where the intrinsic shot noise from the light dominates [8]. For higher signals the FPN surpasses the PSN due to its quadratic dependency. The full-well regime can not be observed here. For the pulse durations that are used here and also in the experiment saturation effects do not play any role. In the experiment the imaging is usually operated with a pulse length of $t_{\text{pulse}} = 25\,\mu\text{s}$. This goes along with a digital count of about $\bar{N}_{\text{count}} = 80$. The ratio of FPN and PSN is calculated as [8]

$$\frac{\sigma_{\text{FPN}}}{\sigma_{\text{PSN}}} = Q_{\text{FPN}} \sqrt{F(e^-/\text{counts}) \cdot N_{\text{counts}}} \quad . \tag{3.12}$$

For the mentioned digital count this is $\frac{\sigma_{\text{FPN}}}{\sigma_{\text{PSN}}} \approx 1.7$. Therefore, FPN is the main contribution to the total noise, while PSN can still not be neglected.

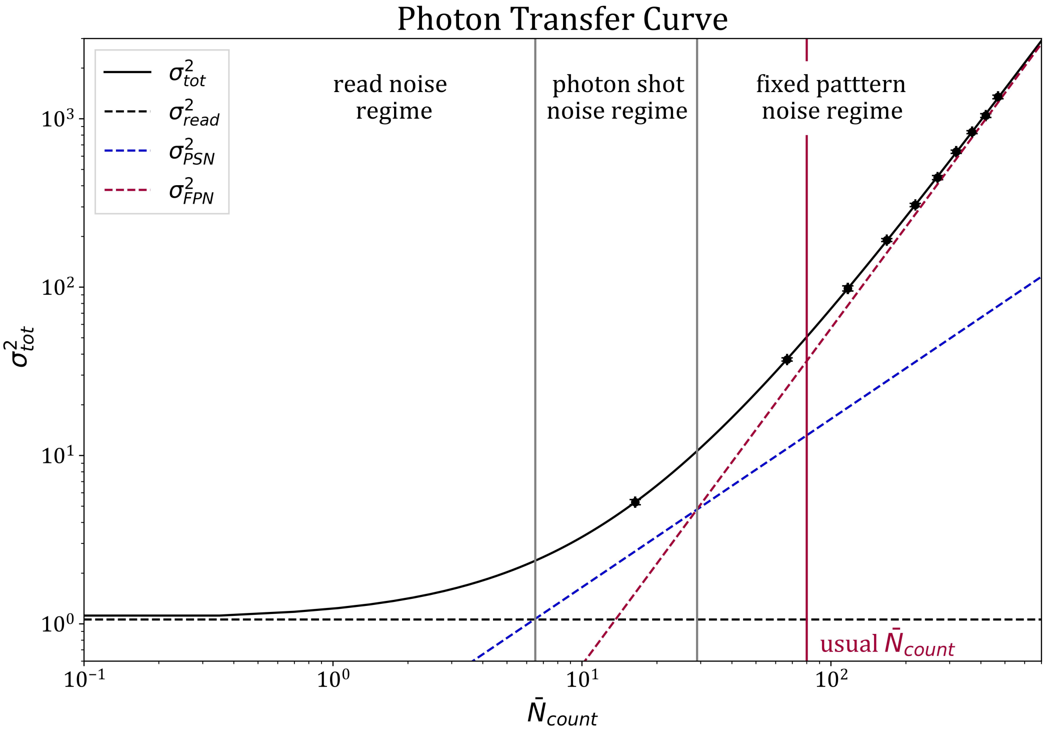

Figure 3.3: PTC for imaging with laser light of a wavelength of 421 nm in a log-log-plot; this exhibits three regimes with a different type of noise dominating: read noise (left), photon shot noise (middle) and fixed pattern noise (right), the mean digital signal usually observed in the experiment is indicated by the red line

In the following two sections we will investigate two types of noise in more detail: the read noise, which is the only type of noise encountered in dark images, and the FPN, which yields the main noise contribution to illuminated images at a pulse duration used in the experiment.

3.4 Read Noise Analysis from Dark Images

Because of the absence of any light source, the dark images, which are taken in each imaging cycle, are only affected by read noise. Therefore, we take a closer look at this particular type of noise and its different components in the following section.
Even without any incident light the sensor creates a signal, the so called dark signal. It can originate from many different sources. One is the thermal excitation of electrons, a process that is indistinguishable from the creation of photoelectrons [2]. The signal can also be produced further down in the process, e.g. in the electronic circuit, where the charge is converted into voltage [8]. The dark signal is not constant but comes with some fluctuation, the read noise represented by the standard deviation of the dark signal σ_{read}. The read noise can be subdivided into dark shot noise and dark fixed pattern noise. For example, the creation of thermal electrons is a random process that follows Poisson statistic and therefore, contributes to the shot noise, whereas the difference in the manufacturing of the electronic circuit of each pixel leads to fixed pattern noise [12]. Dark shot noise and dark fixed pattern noise should not be confused with the PSN and FPN that occur under incident light.
In order to obtain the mean dark signal $\bar{N}_{\text{count, dark}}$ as well as its standard deviation σ_{read} we look at a set of 100 dark images recorded with an exposure time of 2 ms. This setting is also used in the experiment. The digital values N_{count} of all pixels in all images are plotted in a histogram as shown in figure 3.4. To this a Gaussian fit with amplitude A and offset C is applied.

$$G(N_{\text{count}}) = A \cdot \exp\left(-\frac{(\bar{N}_{\text{count, dark}} - N_{\text{count}})^2}{2\sigma_{\text{read}}^2}\right) + C \tag{3.13}$$

For the mean count of the dark signal we obtain $\bar{N}_{\text{count, dark}} = 50.441 \pm 0.010$ and for the standard deviation $\sigma_{\text{read}} = 0.793 \pm 0.014$. How this compares to the result from the PTC is presented after examining the nature of the noise in more detail.

In the following part, we investigate the ratio between the dark shot noise and the dark fixed pattern noise. First, we look at the part of the read noise that follows a fixed pattern. To avoid accounting for the dark shot noise the digital count of each pixel is averaged over the 100 dark images. Since the manufacturing of the pixels slightly differ from one another, this leads to a factor $x_{\text{dark, i}}$ that is constant over time but slightly varies from pixel to pixel [12]. The mean count of a specific pixel is given by

$$\bar{N}_{\text{count, i}} = x_{\text{dark,i}} \cdot \bar{N}_{\text{count, dark}} \quad . \tag{3.14}$$

The factor $x_{\text{dark, i}}$ is obtained by dividing the value of each pixel by the mean value obtained by averaging over all pixel values. As can be seen in figure 3.5 the factor $x_{\text{dark, i}}$ is distributed normally around about 1.

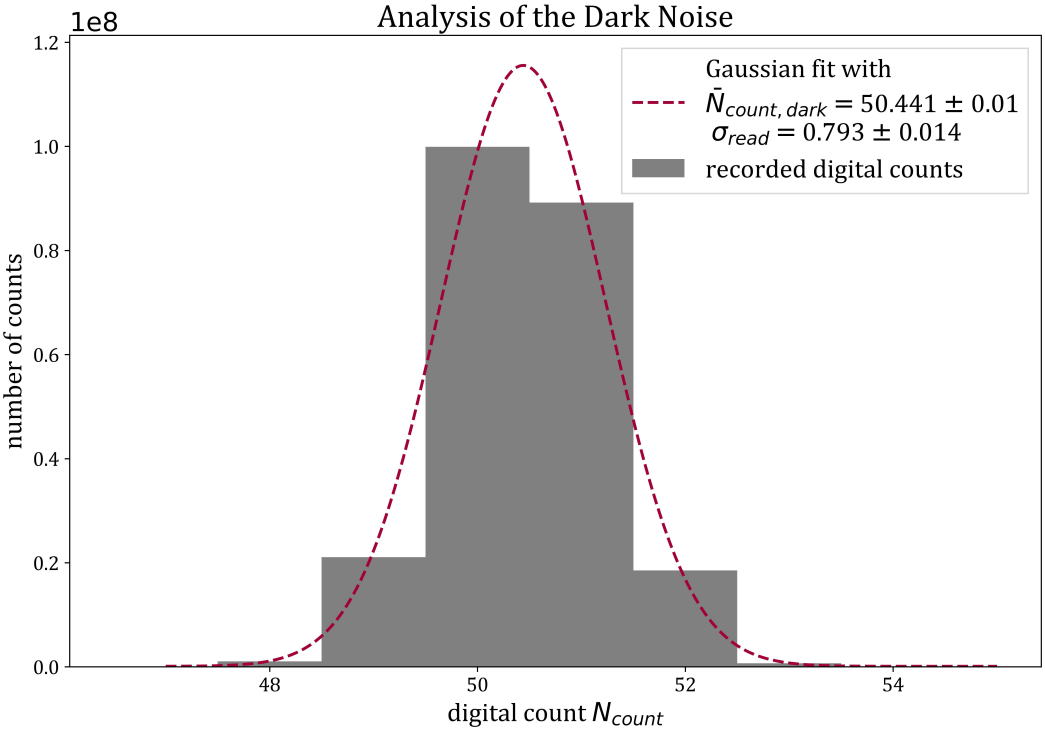

Figure 3.4: Gaussian fit (red) applied to the distribution of the recorded digital counts of each pixel of 100 dark images (grey)

From a Gaussian fit one obtains the mean value $\mu_{\text{x, dark}} = (1.00014.7 \pm 1.3) \cdot 10^{-5}$ and the standard deviation $\sigma_{\text{x, dark}} = (220.9 \pm 1.3) \cdot 10^{-5}$. With this, the read noise that is due to dark fixed pattern noise is calculated as

$$\sigma_{\text{read, FPN}} = \sigma_{\text{x, dark}} \cdot \bar{N}_{\text{count, dark}} \quad . \tag{3.15}$$

We obtain $\sigma_{\text{read, FPN}} = (0.1114 \pm 0.0007)$. This means that about 14 % of all read noise is due to dark fixed pattern noise, whereas the majority of 86 % is due to dark shot noise.

When creating the PTC we subtracted the dark image from the illuminated one. Since the main contribution to the read noise is dark shot noise, we treat the read noise on both images as independent. Because of that, the variance in the PTC due to read noise is about twice of what we found in this section. Transforming the result from this section accordingly leads to a variance of $\sigma^2_{\text{read}} = 1.26 \pm 0.04$. Treating them like this the value we obtain is in a 1σ environment to the one from the PTC. This again confirms that it is reasonable to treat the dark noise as statistically random, a result that will be used in chapter 4.

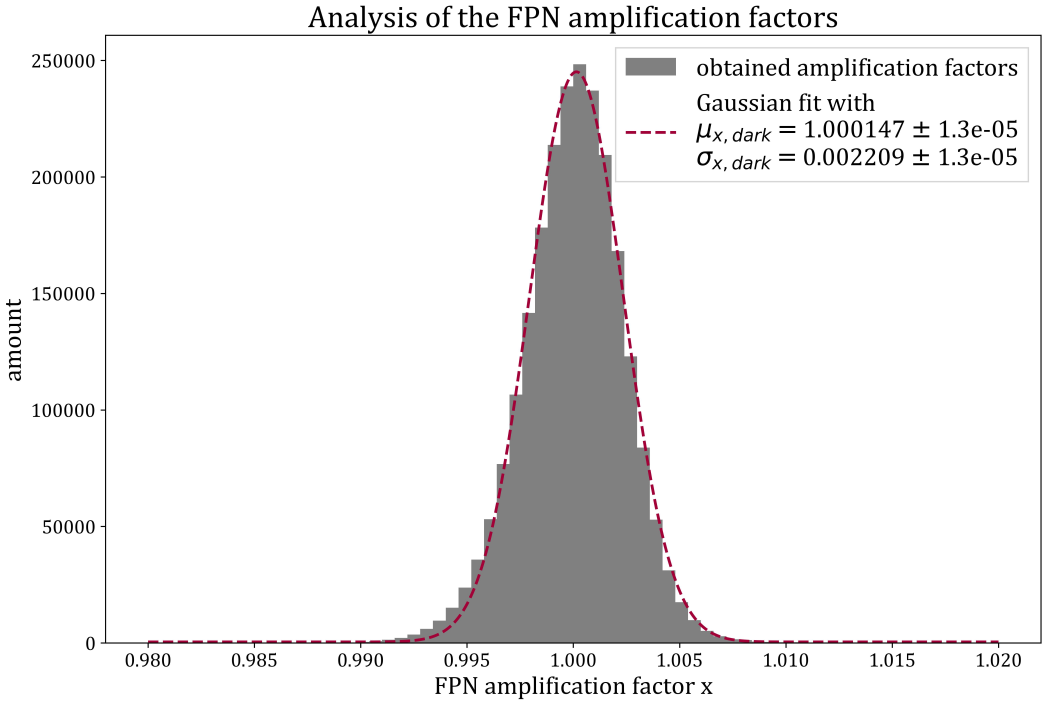

Figure 3.5: Gaussian fit (red) applied to the distribution of the dark fixed pattern noise factor of the pixels after averaging over 100 dark images

3.5 Fixed Pattern Noise Analysis

Since the major part of the total noise for imaging pulse durations of interest comes from FPN, in the present section we will examine this type of noise in more detail. As mentioned before there are different reasons for the appearence of FPN. It can be caused by either the sensor itself or the incident light. The first is referred to as photo response non-uniformity (PRNU). After an electron is hit by a photon the free electrons are collected in the pixels. Due to some slight differences between the manufacturing of the individual pixels, like differences in size, material or the electronic circuit their collecting efficiency differs. This means that there are differences in the sensitivity from pixel to pixel [12]. In the case of CMOS cameras, additionally, there might be differences from row to row, since each row has its own ADC. The second source of FPN is the laser beam. There can be some non-uniformity in the beam profile itself. Furthermore, things like dust along the optical path or on the sensor, might block parts of the light and reflections can cause some interference pattern. All together creates a spatially fixed pattern that is constant over time.

For examining the FPN we take 100 shots that are recorded with a pulse duration of $t_{\text{pulse}} = 25\,\mu$s, subtract the dark image and then average over all 100 shots. We now look at a subarray of 300×300 pixels centered around the position of the atomic cloud. The obtained image is shown in figure 3.6. Besides the small spherical interference pattern caused by some dirt, there is also a pattern of almost horizontal lines. A similar pattern was observed in [8] where it was attributed to reflections between the sensor's surface and the optical window.

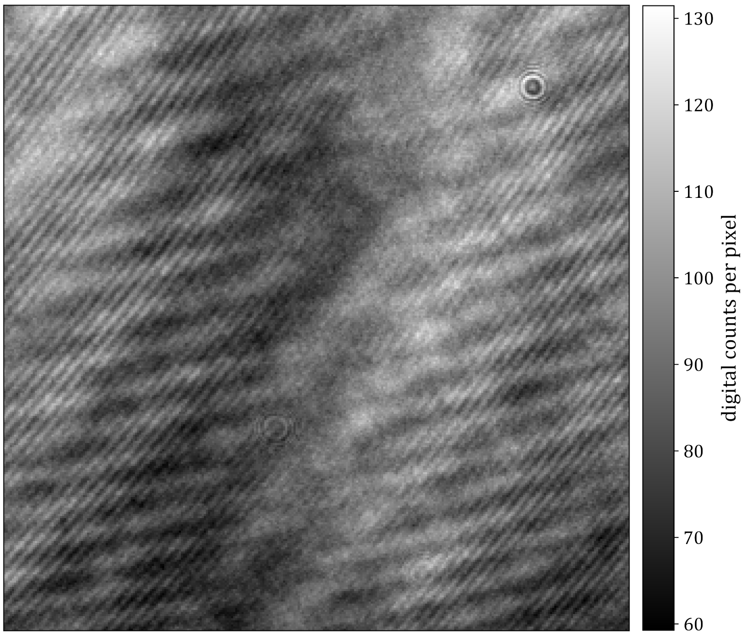

Figure 3.6: image of size 300 × 300 pixels created from averaging over 100 shots that were illuminated under conditions present in the experiment

We now look at the distribution of the fixed pattern factor $x_{\mathrm{FPN,\ i}}$ that is individual to each pixel and is expected to be distributed around 1 [12]. The number of counts per pixel is given by

$$\bar{N}_{\mathrm{count,i}} = x_{\mathrm{FPN,i}} \cdot \bar{N}_{\mathrm{count}} \quad . \tag{3.16}$$

To obtain the fixed pattern factor of each pixel we divide the value of each pixel by the mean obtained over all pixels. The distribution of the amplification factors is almost Gaussian with a standard deviation of $\sigma_{\mathrm{x,\ FPN}} = 0.1289 \pm 0.0011$. This quantity is equivalent to the FPN quality factor Q_{FPN}. Its value is significantly higher than the one obtained from the PTC. This is probably due to the large difference in the size of the considered areas, which are 300 × 300 pixels and 10 × 10 pixels respectively. For a larger area the light intensity patterns are more distinct and it is more likely that the counts per pixel differ over a wider range.

Now we want to investigate the part of the FPN that is due to PRNU, which is denoted as σ_{PRNU}. Equivalent to equation 3.6 the PRNU quality factor Q_{PRNU} is introduced. [8]

$$\sigma_{\mathrm{PRNU}} = Q_{\mathrm{PRNU}} \cdot \bar{N}_{\mathrm{count}} \tag{3.17}$$

In order to calculate its value, one should illuminate the sensor with perfectly uniform light and create a flatfield image out of that. It is not possible to create such a beam that has a large enough size with the laser that is used in the set-up, since the high coherence makes it hard to avoid the creation of interference patterns. Because of that, a smartphone light is used to illuminate the sensor. However, note that the FPN can show a wavelength dependency [8] and the present result has to be taken with a grain of salt.

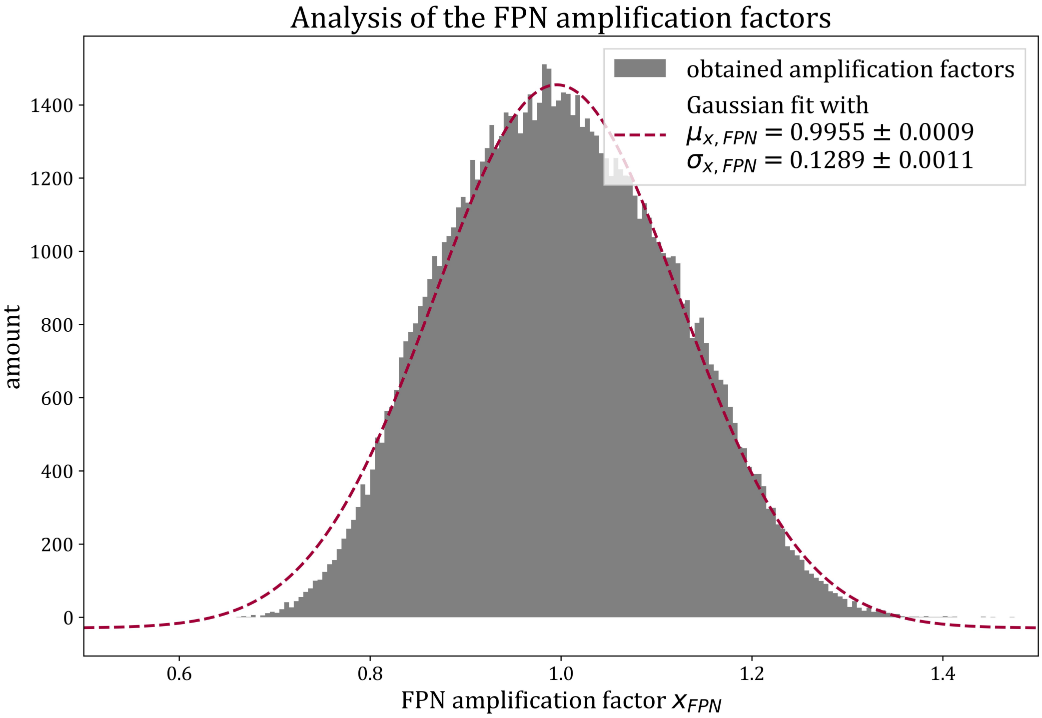

Figure 3.7: Gaussian fit (red) applied to the distribution of the FPN amplification factors from 300 × 300 pixels illuminated with a laser pulse of 25 μs, averaged over 100 images

The flatfield image is obtained by averaging over 100 single shots. Since there is still some gradient in the brightness of the light, we look at a slightly smaller subarray of 100 × 100 pixels centered around the position of the atomic cloud. The image is shown in figure 3.8. One can see some single pixels that are significantly brighter than the others. That there is more fluctuation between the rows than the columns can not be observed.

From here we proceed as described in section 3.4. The distribution of x_{PRNU} is shown in 3.9. We get a standard deviation of $\sigma_{\text{x, PRNU}} = (3.27 \pm 0.04) \cdot 10^{-3}$. This is again equivalent to the PRNU quality factor. The obtained value is in accordance with an expected value below 1 % as observed in [8]. With Q_{PRNU} we can calculate the noise due to PRNU using equation 3.17. With a digital count of usually around 80 for the pulse duration used in the experiment after subtracting the dark image we obtain $\sigma_{\text{PRNU}} = 0.261 \pm 0.003$. This is only about 4 % of the total FPN $\sigma_{\text{FPN}} = 6.032 \pm 0.024$. This indicates that the main contribution to FPN is not the difference in the sensitivity of the pixels but rather the non-uniform illumination of the sensor.

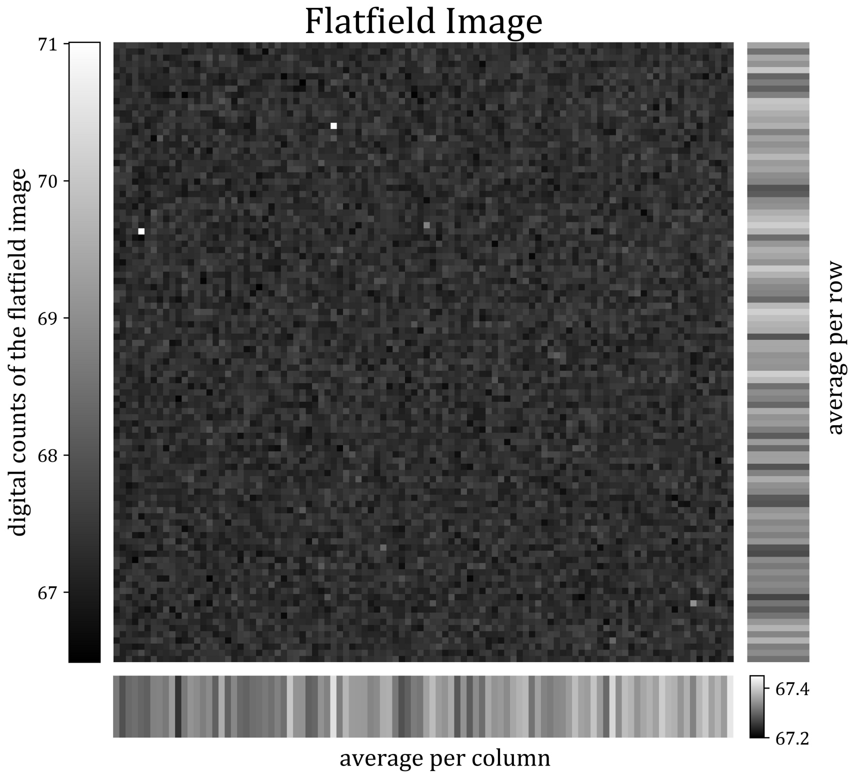

Figure 3.8: flat-field image of size 100 × 100 pixels created from averaging over 100 shots that are illuminated by uniform light from a smartphone, model Samsung Galaxy S21 FE 5G; the diagrams at the bottom and right show the average digital count per column and row

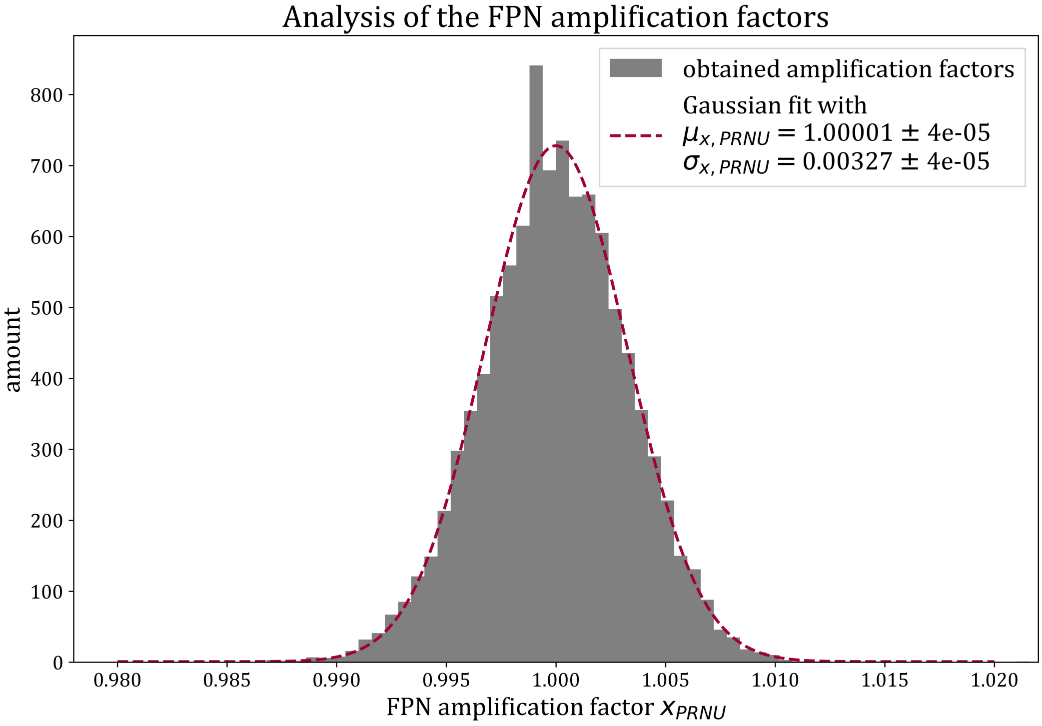

Figure 3.9: Gaussian fit (red) applied to the distribution of the FPN amplification factors that are obtained after averaging over 100 uniformly illuminated shots

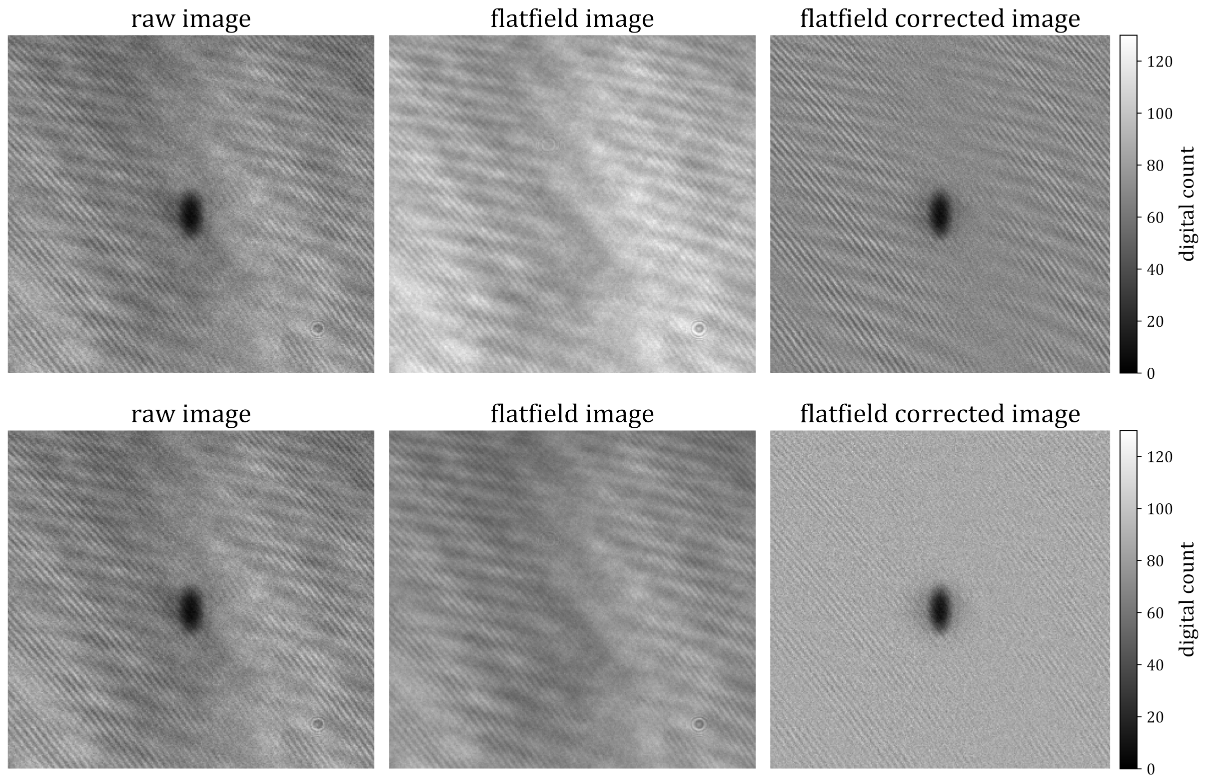

Figure 3.10: raw image of the atomic cloud, which is taken with $t_{\text{pulse}} = 20\,\mu\text{s}$ and of which the dark image is subtracted (left); corrected by normalizing it by a flat-field image (center); the flat-field image is created out of 100 shots of $t_{\text{pulse}} = 25\,\mu\text{s}$ (top) or 10 shots of $t_{\text{pulse}} = 20\,\mu\text{s}$ (bottom); result (right)

3.6 Flat Fielding

The following section deals with the topic of noise reduction. As exhibited before neither the full-well nor the read noise contribute to the total noise in a notable way for a pulse duration of interest. Therefore, the only relevant types of noise are PSN and FPN. Since PSN represents an intrinsic limitation to imaging the only part that can be improved is the FPN. To do this, we apply the method of flat fielding to the images as described in [8]. The idea is to create a flat-field image by averaging over a large number of images taken under the same conditions. Therefore, the flat-field image contains the fixed pattern but no PSN. It is used to normalize the raw image. The raw image is divided by the flat field image pixel by pixel and than multiplied by the average digital count of the flat-field image $\bar{N}_{\text{count, flatfield}}$. From this one obtains the corrected digital count per image $N_{\text{count, i, corr}}$.

$$N_{\text{count, corr, i}} = \bar{N}_{\text{count, flatfield}} \frac{N_{\text{count, i}} - N_{\text{count,dark,i}}}{N_{\text{count, flatfield, i}}} \tag{3.18}$$

We test two different methods to obtain the flat-field image. In the first method, independent from the imaging pulse duration in the absorption image we use the average of 100 shots recorded with a laser pulse duration of $t_{\text{pulse}} = 25\,\mu\text{s}$ after subtracting the dark image from each. In the second, we create the flat-field image from an average over 10 shots recorded with the same pulse duration, from which a dark image was subtracted, and apply this only to raw images taken with the same pulse duration. An example of what applying such a flat-field image to an image of the atomic cloud looks like is shown in figure 3.10. In both cases larger patterns as well as the circular interference pattern in the lower right corner could be removed to some extent. For the second case that works clearly better than for the first. Still, in both images there remain some small diagonal fringes.

By again creating a PTC that is displayed in figure 3.11 one can see, that the noise is reduced significantly. The FPN quality factor has dropped from (0.0754 ± 0.0003) to (0.0514 ± 0.0004) in the first case and to (0.0389 ± 0.0005) in the second. This corresponds to a reduction of the FPN of about 30 % and 50 % respectively. Therefore, also the noise regimes shift. Looking at a mean count of 80, in the first case, variance due to FPN has dropped from about 70 % of the total variance to 55 %, while the PSN is responsible for 40 % and the read noise for 5 %. In the second case, the FPN is only responsible for 39 %, while photon shot noise and read noise make up for 54 % and 7 % respectively.

As a conclusion, one can say that by applying flat fielding it is possible to reduce FPN to an extent where PSN becomes the dominant noise. Still the FPN is not small enough to be neglected.

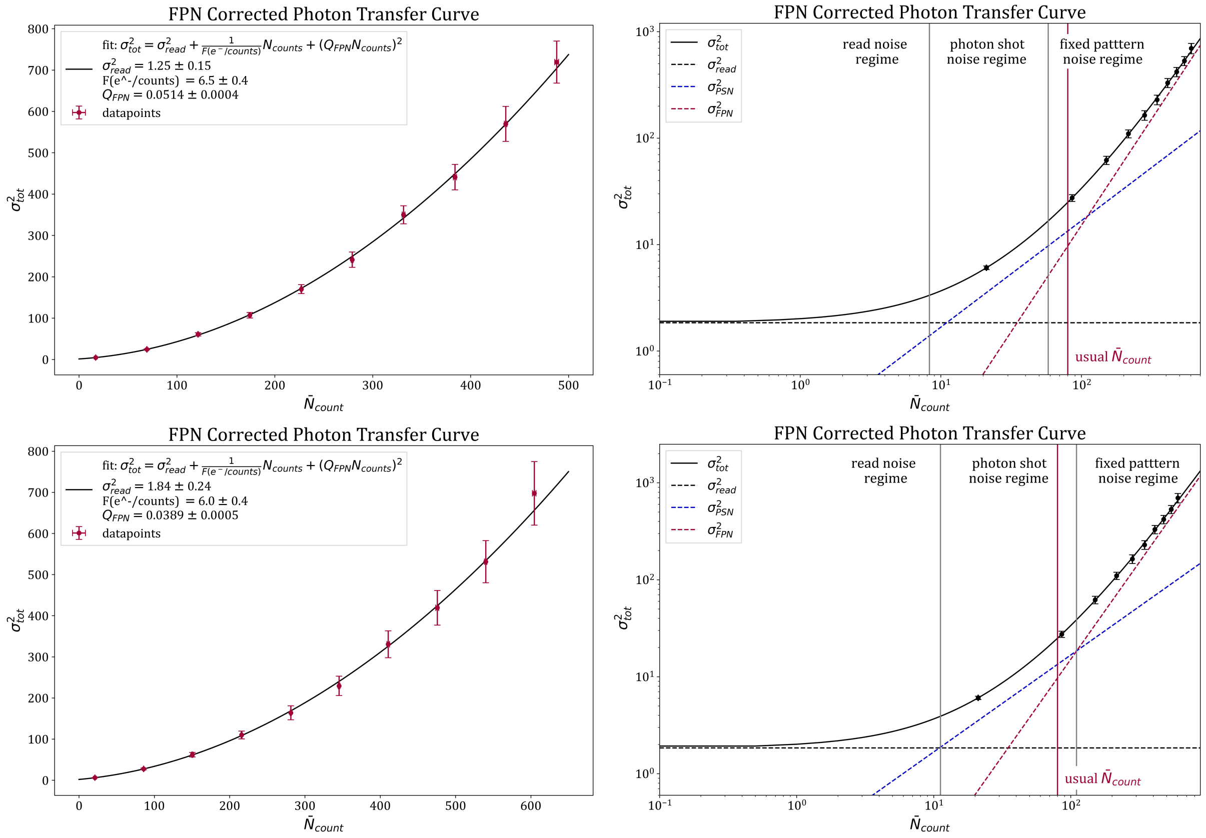

Figure 3.11: PTCs for flat fielding applied images; the flat-field image is created out of 100 shots of $t_{\text{pulse}} = 25\,\mu\text{s}$ (top) or 10 shots of adjusted pulse duration (bottom); the fit values from a second order polynomial fit are displayed (left) as well as the different noise regimes (right); the red vertical line indicates the usual mean digital count observed in the experiment

Chapter 4

Simulation of Absorption Imaging

4.1 Derivation of the Density Distribution

In order to simulate the image of the atomic cloud it is necessary to know the distribution of the atoms projected on a two dimensional plane, i.e. the column density. After giving the general formula we will express the column density in terms of quantities that are accessible in the experiment.

In our case, the imaging is conducted along the x-axis. The observed cloud normally consists of a BEC and a thermal cloud, which are confined in a harmonic potential. In the Thomas-Fermi limit where the interaction between the atoms are much stronger than the confining potential the column density of the condensate can be described as [15]

$$n_c(y,z) = n_{c,0} \cdot \max\left(0\,,\, 1 - \frac{y^2}{R_{c,y}^2} - \frac{z^2}{R_{c,z}^2}\right)^{3/2} \tag{4.1}$$

with the condensates peak column density $n_{c,0}$ and its extension in y (z) direction $R_{c,y}$ ($R_{c,z}$). The column density of the thermal cloud is given by [15]

$$n_{th}(y,z) = n_{th,0} \cdot g_2\left(\exp\left(-\frac{y^2}{R_{th,y}^2} - \frac{z^2}{R_{th,z}^2}\right)\right) \tag{4.2}$$

where $g_s(l) = \sum_{k=1}^{\infty} \frac{l^k}{k^s}$ denotes the Polylogarithm. The cloud is characterized by its peak column density $n_{th,0}$ as well as its radial extension $R_{th,y,z}$ in the y,z-plane. Different from the condensate the edge of the thermal cloud is not well defined, since the polylog term in 4.2 never reaches 0 as can be seen in figure 4.1. However, in first order it can be approximated as a Gaussian distribution. Therefore, the radius of the cloud corresponds to $\sqrt{2}$ times the standard deviation of the corresponding normal distribution.

The densities of thermal and condensed part simply add up to the total column density [15].

$$\begin{aligned} n_{tot}(y,z) &= n_c(y,z) + n_{th}(y,z) \qquad (4.3)\\ &= n_{c,0} \cdot \max\left(0\,,\, 1 - \frac{y^2}{R_{c,y}^2} - \frac{z^2}{R_{c,z}^2}\right)^{3/2} + n_{th,0} \cdot g_2\left(\exp\left(-\frac{y^2}{R_{th,y}^2} - \frac{z^2}{R_{th,z}^2}\right)\right) \qquad (4.4)\end{aligned}$$

We now want to find an expression for equation 4.4 that does not depend on peak densities and radii but on parameters that are accessible in the experiment, such as temperature T, condensate fraction f, total atom number N, trapping frequencies $\omega_{x,y,z}$, scattering length a and time of flight t_{tof}. Because of the bimodality of equation 4.4 we can look at each part individually [10] starting with the thermal cloud.

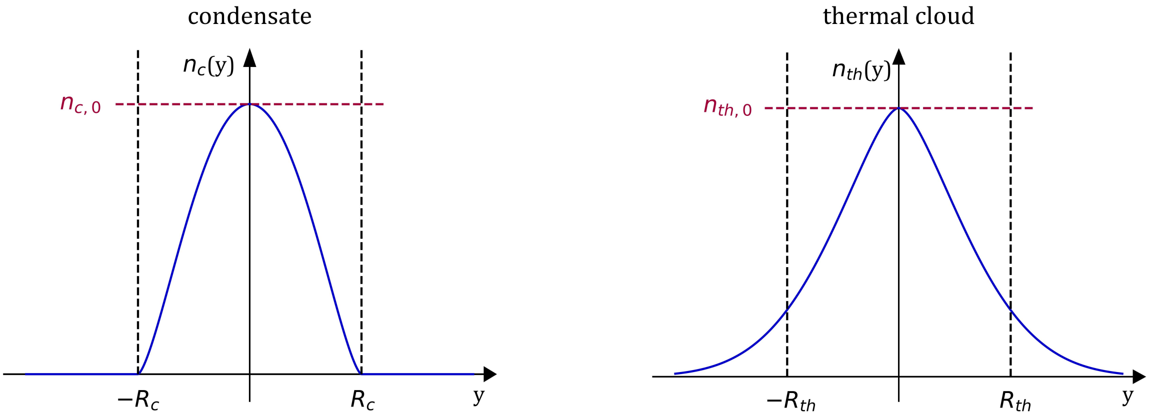

Figure 4.1: schematic cross section through the density distribution of a condensate (left) and a thermal cloud (right)

The atomic cloud is trapped in a confining potential that is approximately harmonic

$$V_{ext} = \frac{1}{2}m\omega_x^2x^2 + \frac{1}{2}m\omega_y^2y^2 + \frac{1}{2}m\omega_z^2z^2 \tag{4.5}$$

with ω_x (ω_y, ω_z) denoting the trapping frequencies in x (y, z) direction and m being the mass of one Dy atom. Therefore, we have the following relation for the size of the thermal cloud $R_{th,x,y,z}(t=0)$ which is still trapped, i.e. before the time of flight.

$$V_{ext} = \frac{1}{2}m\omega_{x,y,z}^2R_{th,x,y,z}^2(t=0) \tag{4.6}$$

Treating the thermal cloud as classical gas one obtains the following relation from the equipartition theorem

$$\frac{1}{2}k_BT = \frac{1}{2}m\left\langle v^2\right\rangle = \frac{1}{2}m\omega_{x,y,z}^2\left\langle R_{th,x,y,z}^2(t=0)\right\rangle \tag{4.7}$$

with k_B being the Boltzmann constant. The expression $\left\langle v^2\right\rangle$ stands for the mean of the squared velocity of the atoms in radial direction and $\left\langle R_{th}^2(t=0)\right\rangle$ for the mean squared radial distance of the atoms at $t=0$. The size of the thermal cloud after a time of flight depends on its initial size, the variance of their initial velocity and the duration of free flight.

$$R_{th,x,y,z}^2(t=t_{tof}) = \left\langle R_{th,x,y,z}^2(t=0)\right\rangle + \left\langle v^2\right\rangle \cdot t_{tof}^2 \tag{4.8}$$

From equation 4.7 we obtain the following relations.

$$\left\langle R^2_{th,x,y,z}(t=0)\right\rangle = \frac{k_B T}{m\omega^2_{x,y,z}} \qquad \left\langle v^2\right\rangle = \frac{k_B T}{m} \tag{4.9}$$

Inserting them into equation 4.8 yields

$$R_{th,x,y,z}(t=t_{tof}) = \sqrt{\frac{k_B T}{m}\left(\frac{1}{\omega^2_{x,y,z}} + t^2_{tof}\right)} \quad . \tag{4.10}$$

Now we still need the peak density of the thermal cloud. The total number of atoms in the thermal cloud N_{th} is given by integrating over the column density distribution.

$$N_{th} = n_{th,0}\int_{-\infty}^{\infty}\int_{-\infty}^{\infty} g_2\left(\exp\left(1-\frac{y^2}{R^2_{th,y}}-\frac{z^2}{R^2_{th,z}}\right)\right)\mathrm{dy}\,\mathrm{dz} \tag{4.11}$$

Setting this equal to $N_{th} = (1-f)N$ provides an expression for the peak density.

$$n_{th,0} = (1-f)N\left[\int_{-\infty}^{\infty}\int_{-\infty}^{\infty} g_2\left(\exp\left(1-\frac{y^2}{R^2_{th,y}}-\frac{z^2}{R^2_{th,z}}\right)\right)\mathrm{dy}\,\mathrm{dz}\right]^{-1} \tag{4.12}$$

In the simulation this is solved numerically setting the boundaries of the integral to $6/\sqrt{2}$. This is equivalent to $6\,\sigma$ of a corresponding Gaussian distribution. Integration up to this point excludes less than $2\cdot 10^{-7}\,\%$ of all values.

Now we also want to rewrite the density distribution of the condensate. As a starting point we use the Gross-Pitaevskii equation, which adds a term for the interaction of particles $g|\phi^3(x,y,z,t)|^2$ to the Schrodinger equation [3].

$$i\hbar\frac{\partial}{\partial t}\Phi(x,y,z,t) = \left(-\frac{\hbar^2\nabla^2}{2m} + V_{ext}(x,y,z) + g|\Phi(x,y,z,t)|^2\right)\Phi(x,y,z,t) \tag{4.13}$$

The ground state wave function is given by $\Phi(x,y,z,t) = \phi(x,y,z)e^{-i\mu t}$. Its amplitude $\phi(x,y,z)$ is real and normalized to the atom number in the condensate N_c. The chemical potential is indicated by μ [10]. The confining potential can be described by equation 4.5. The coupling constant g is given by [3]

$$g = \frac{4\pi\hbar^2 a}{m} \quad . \tag{4.14}$$

where $\hbar$ denotes the reduced Planck constant. In this experiment the scattering length a is in the order of $a \approx 300\,a_0$, where a_0 denotes the Bohr radius. In the Thomas-Fermi approximation the kinetic energy is neglected and equation 4.13 leads to an expression for the chemical potential.

$$\mu = V_{ext}(x,y,z) + g|\Phi(x,y,z,t)|^2 \tag{4.15}$$

The chemical potential depends on the number of particles in the condensate $N_c = f\cdot N$ and the confining potential. Before the time of flight its mean is given by

$$\bar{\mu}(t=0) = \frac{\hbar\bar{\omega}}{2}\left(\frac{15N_c a}{\bar{a}_{ho}}\right)^{2/5} \tag{4.16}$$

and its spatial dependence accordingly by

$$\mu_{x,y,z}(t=0) = \frac{\hbar\omega_{x,y,z}}{2}\left(\frac{15N_c a}{a_{ho,x,y,z}}\right)^{2/5} \tag{4.17}$$

with

$$\bar{a}_{ho} = \sqrt{\frac{\hbar}{m\bar{\omega}}} \qquad \text{and} \qquad a_{ho,x,y,z} = \sqrt{\frac{\hbar}{m\omega_{x,y,z}}} \tag{4.18}$$

denoting the typical length scale of the trap [3]. After the condensate is released from the trap, its chemical potential scales with time as [10]

$$\mu_{x,y,z}(t) = \frac{\mu_{x,y,z}(t=0)}{1+\omega_{x,y,z}^2 t^2} \tag{4.19}$$

We now look at the edge of the condensate $R_{c,x,y,z}$, where the density becomes 0 and therefore the last term of equation 4.15 vanishes. Expression 4.18 is inserted into equation 4.19 and with this 4.15 is solved for $R_{c,x,y,z}$ setting the time to $t = t_{tof}$. We obtain the following expression for the radius of the condensate after a time of flight.

$$R_{c,x,y,z} = \sqrt{\frac{\hbar\omega_{x,y,z}}{m}}\left(\frac{15N_c a}{a_{ho,x,y,z}}\right)^{1/5}\sqrt{\frac{1+\omega_{x,y,z}^2 t_{tof}^2}{\omega_{x,y,z}^2}} \tag{4.20}$$

The peak density of the cloud is located in the center where $x = y = z = 0$. Therefore, the first term on the right of equation 4.15 vanishes and we get an expression for the peak density of the condensate in three dimensions $n_{c,0}^{3D}$.

$$n_{c,0}^{3D}(t) = |\Phi(x,y,z,t)|^2 = \frac{\bar{\mu}(t)}{g} \tag{4.21}$$

Integration along the x-axis returns the peak column density.

$$n_{c,0} = \frac{4}{3}R_{c,x}\frac{\bar{\mu}(t)}{g} = \frac{4}{3}R_{c,x}\frac{1}{g}\frac{\hbar\bar{\omega}}{2}\left(\frac{15N_c a}{\bar{a}_{ho}}\right)^{2/5}\frac{1}{(1+\omega_x^2 t_{tof}^2)^{1/2}}\frac{1}{(1+\omega_y^2 t_{tof}^2)^{1/2}}\frac{1}{(1+\omega_z^2 t_{tof}^2)^{1/2}} \tag{4.22}$$

With this we have all the relations to replace $n_{th,0}$, $R_{th,y}$, $R_{th,z}$ $n_{c,0}$, $R_{c,y}$ and $R_{c,z}$ in the total column density as given in equation 4.4 by the experimentally accessible quantities T, f, N, $\omega_{x,y,z}$, a and t_{tof}.

4.2 Simulation Procedure

In order to simulate the imaging process we adapt the code developed by Felix Borchers [1] to the situation in our experiment, i.e. we implement the density distribution that describes a cloud of bosonic atoms at low temperatures in terms of experimentally accessible quantities. The code for this can be found in appendix A.3. Furthermore, we feed in the characteristics of the noise that were determined before. The following paragraph will give an overview of the simulation procedure. A schematic overview of the program's working principle is shown in figure 4.2. For more details please refer to [1].

As presented in section 1.3 in order to obtain the OD three different pictures are taken: a dark image, one were the camera is illuminated without an atomic cloud, the so called background image, and one were the atoms are present, the absorption image. This is replicated in the simulation. Each of the three virtual images is created by using a two dimensional array, of which each entry corresponds to the count in one pixel. We consider both the mean signal and the effects of the different noise sources described in chapter 3.

To the dark image only read noise is applied. In section 3.4 we have shown that the fixed pattern part of the read noise only plays a minor role. Therefore, for every entry in the array random values are created that are distributed normally around 50.441 with a standard deviation of 0.793, which is in accordance with what we observed.

To simulate the illuminated images, we start with the incoming light in terms of intensity. One uses an average over 100 real background images of which the dark image was subtracted and translate these into units of intensity. With this we account for the main part of the FPN, which is caused by non-uniform illumination of the camera due to e.g. interference, as shown in section 3.6.

For the absorption image we simulate the absorption process by applying formula 1.1 using the results derived in section 4.1 for the column density distribution n_{tot}.

$$I_{det}(y,z) = I_0(y,z)\exp\left(-\sigma_0 n_{tot}(y,z)\right) \tag{4.23}$$

The intensity of both illuminated images is now translated into the average number of photons $\bar{N}_{ph}$ per simulated pixel via

$$\bar{N}_{ph} = \frac{I \cdot A_{\text{eff}} \cdot t_{pulse}}{hc/\lambda} \tag{4.24}$$

with c being the speed of light and h being the Planck constant. The effective area of one pixel in the plane of the atomic cloud is $A_{\text{px, eff}} = 7.47\,\mu\text{m}^2$ in the present case. To the average number of photons hitting a virtual pixel the photon shot noise is applied by creating random values for each virtual pixel Poisson distributed around the mean number of photons. Now the number of photons is transferred into digital counts by

$$N_{\text{count}} = \frac{N_{ph} \cdot QE}{F(e^-/\text{counts})} \tag{4.25}$$

taking the quantum efficiency (QE) into account. To this the dark signal with read noise is added. The result is rounded to integer values. The final image in units of digital counts is calculated from the three images via equation 1.5 and then transferred into OD by equation 1.6.

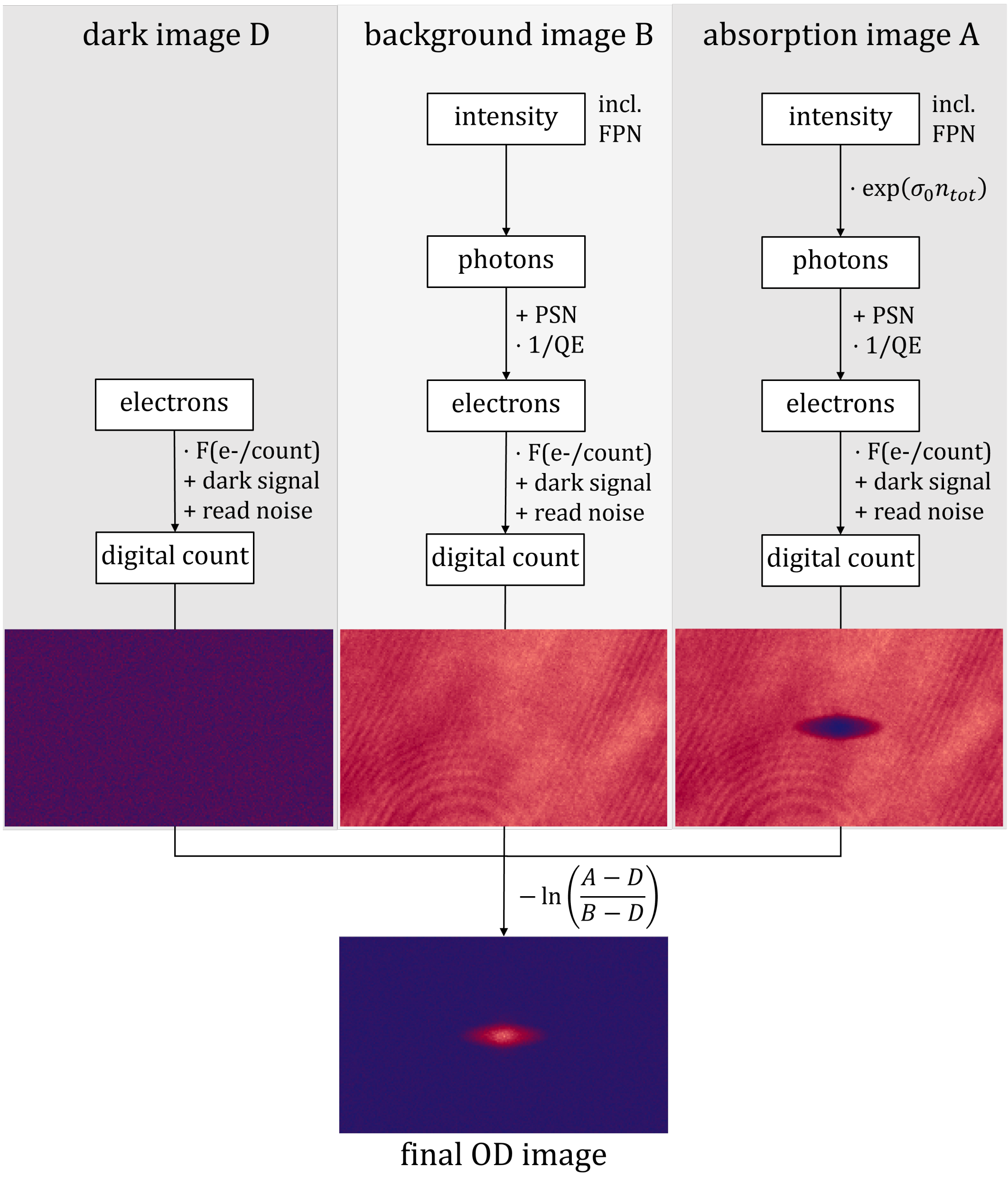

Figure 4.2: schematic representation of the simulation of absorption imaging

4.3 Reliability of the fit

Finally, we want to investigate the reliability of the fit routine that is used in the experiment and which was developed by Jianshun Gao und Joschka Schöner. In the fit routine formula 4.4 is applied to the OD images. From this the macroscopic quantities characterising the cloud are extracted. For checking the reliability of the fit we create sets of simulated OD images of which we know the input parameters and then compare these to the fit result. An example of the application of a fit to a simulated atomic cloud can be found in figure 4.3. From the fit we obtain values for size and density of the atomic cloud in terms of number of pixels and digital counts. These must be converted back into physical units. The radii are converted by multiplying the number of counts by the effective pixel size in the plane of the atomic cloud $d_{\text{eff}} = 2.733\,\mu\text{m}$.

$$R_{th}[\text{m}] = R_{th}[\text{px}] \cdot d_{\text{eff}} \qquad R_{c,y,z}[\text{m}] = R_{c,y,z}[\text{px}] \cdot d_{\text{eff}} \tag{4.26}$$

To convert digital counts into number of atoms, we introduce the conversion factor $F(\text{count/atoms})$.

$$F(\text{count/atoms}) = \frac{1}{\sigma_0} \cdot A_{\text{eff}} \tag{4.27}$$

In the present case is $F(\text{count/atoms}) \approx 176.5$. With this we obtain the number of atoms in the condensate as well as the thermal cloud by integrating, i.e. summing over the digital counts in the respective distributions.

$$N_{th}[\text{atoms}] = F(\text{count/atoms}) \cdot \sum n_{th}(R_{th}[\text{counts}]) \tag{4.28}$$

$$N_c[\text{atoms}] = F(\text{count/atoms}) \cdot \sum n_c(R_{c,y}[\text{counts}], R_{c,z}[\text{counts}]) \tag{4.29}$$

With the extension of the cloud and the number of atoms in physical units we can derive further quantities, explicitly total atom number, condensate fraction, temperature and scattering length, by using the results from section 4.1.

$$N = N_{th} + N_c \tag{4.30}$$

$$f = \frac{N_c}{N_c + N_{th}} \tag{4.31}$$

$$T = R_{th}^2 \frac{m}{k_B} \left(\frac{1}{\bar{\omega}^2} + t_{tof}^2 \right)^{-1} \tag{4.32}$$

$$a = \frac{R_{c,y,z}^5 a_{ho,y,z}}{15 N_c} \left(\frac{\hbar \omega_{y,z}}{m} \frac{1 + \omega_{y,z}^2 t_{tof}^2}{\omega_{y,z}^2} \right)^{-5/2} \tag{4.33}$$

It is assumed that the time of flight and the trapping frequencies are known.

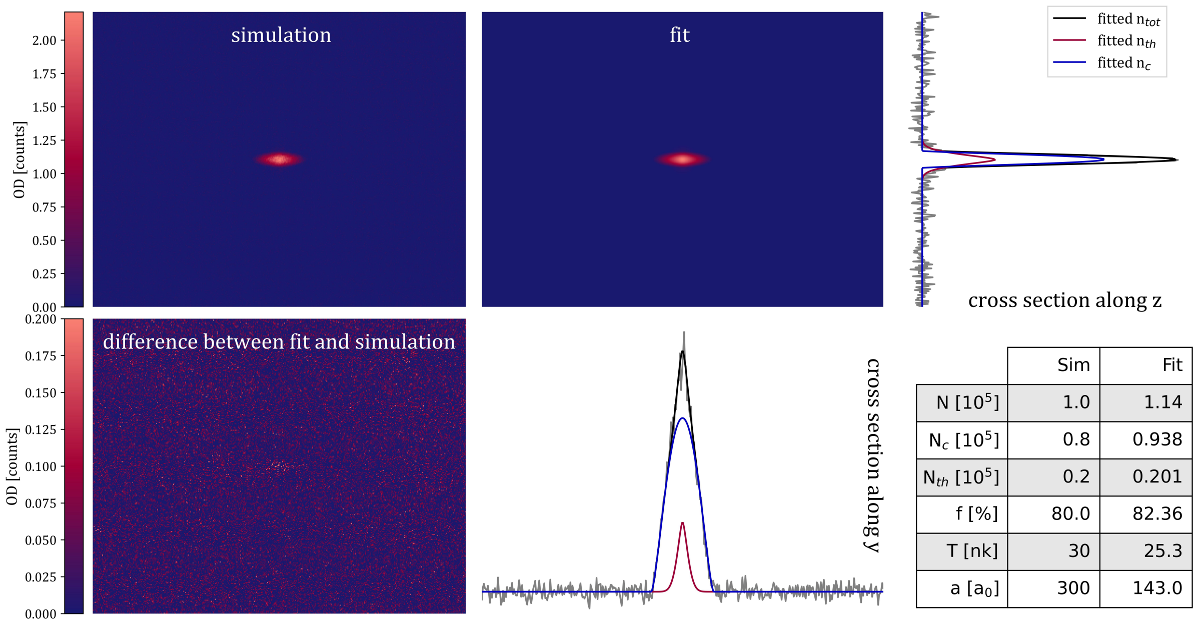

	Sim	Fit
N [10^5]	1.0	1.14
N_c [10^5]	0.8	0.938
N_{th} [10^5]	0.2	0.201
f [%]	80.0	82.36
T [nk]	30	25.3
a [a_0]	300	143.0

Figure 4.3: (top left) simulated column density distribution of a partly condensed cloud; (top center) applied fit; (bottom left) residue; (top right, bottom center) cross sections through the simulated distribution with applied fits; (bottom right) comparison of the input parameters and the fit results

The following part compares fit results and input parameters for different sets of simulations. The goal is to make a statement on the reliability of the fit in different experimental situations. First, we look at different condensate fractions. In the experiment there are two situations that are particularly interesting. On the one hand, the transition into condensation with condensate fractions between 0 and 10 % and on the other hand an atomic cloud where there is almost pure condensate with condensate fractions between 70 and 100 %. In the first case, we usually have trapping frequencies of $\omega_x = 2\pi \cdot 206$ Hz, $\omega_y = 2\pi \cdot 96$ Hz and $\omega_z = 2\pi \cdot 227$ Hz, temperatures of about $T = 300\,\text{nK}$ and total atom numbers of $N = 3 \cdot 10^5$. In the second case, the trapping frequencies are $\omega_x = 2\pi \cdot 45$ Hz, $\omega_y = 2\pi \cdot 10$ Hz and $\omega_z = 2\pi \cdot 126$ Hz, the temperature is about $T = 30$ nK and the total atom number $N = 1 \cdot 10^5$. In both cases, we use a time of flight of $t_{tof} = 20\,\text{ms}$ and assume a scattering length of $a = 300\,a_0$. We create 10 simulations for each set of parameters and apply the fit routine to each of them. From that we extract condensate fraction, total atom number, temperature and scattering length and calculate the mean for the 10 sets. The errorbars correspond to the standard error. The result is shown in figure 4.4 and 4.5.

For low condensate fractions f is determined relatively precisely. An exception is the absence of any BEC. Here a small condensate is fitted anyway. Also for high condensate fractions the estimate is precise. However, the case of pure BEC is not identified as such.

When it comes to the total atom number there is an almost constant underestimate of about 3 % for low as well as high condensate fractions. In the first case, there are about 8000 atoms missing in the thermal cloud, in the second case, about 3000 atoms in the condensate. This means that in both cases the atom number of the larger part is slightly underestimated.

The temperature tends to be slightly overestimated by up to 5 nK in the case of low condensate fractions. For high condensate fractions the result is pretty precise except for very high f above about 92 %. This is only logical, since T is derived from the thermal part of the atomic cloud. Finally, the scattering length is determined from the condensed part. We observe a distribution around $300\,a_0$ for low condensate fractions with deviations up to about 15 %. Because of $a \propto R^5_{c,y,z}/N_c$, slight deviations in fitting the size of the condensate can cause significant false estimates of the scattering length. Since fitting very low condensate fractions for single simulations can result in extremely high scattering lengths and therefore distort the result, such cases were excluded when calculating the mean. Hence, one must note that the determination of a is not very reliable. In the case of high condensate fractions, there is a constant overestimate of about 4 %. This corresponds to the slight underestimate of the condensates atom number.

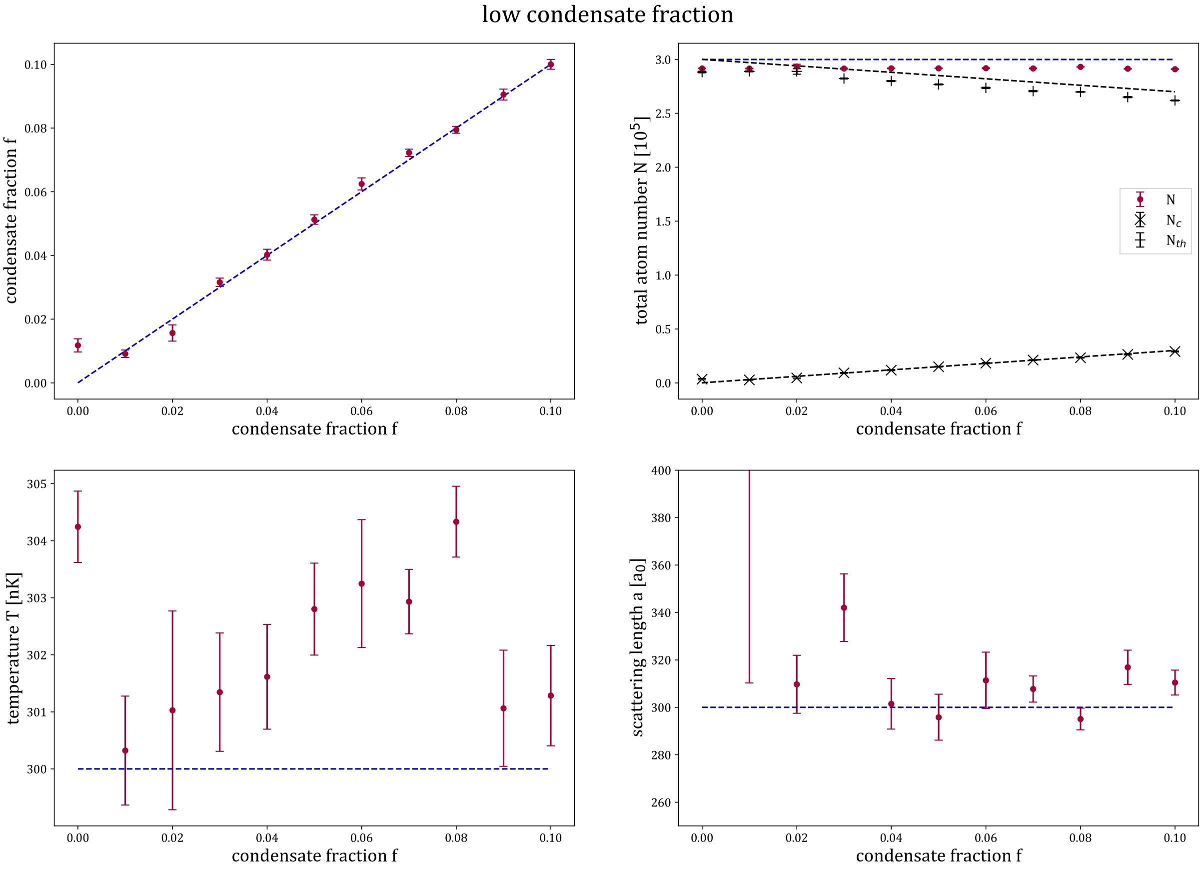

Figure 4.4: (red) mean values for condensate fraction (top left), total atom number (top right), temperature (bottom left) and scattering length (bottom right) obtained by applying the fit routine used in the experiment to 10 simulations for each condensate fraction from 0 to 10 %; (blue) expected values as fed into the simulations for trapping frequencies $\omega_{x,y,z} = 2\pi \cdot (206, 96, 227)$ Hz and a time of flight $t_{\text{tof}} = 20$ ms

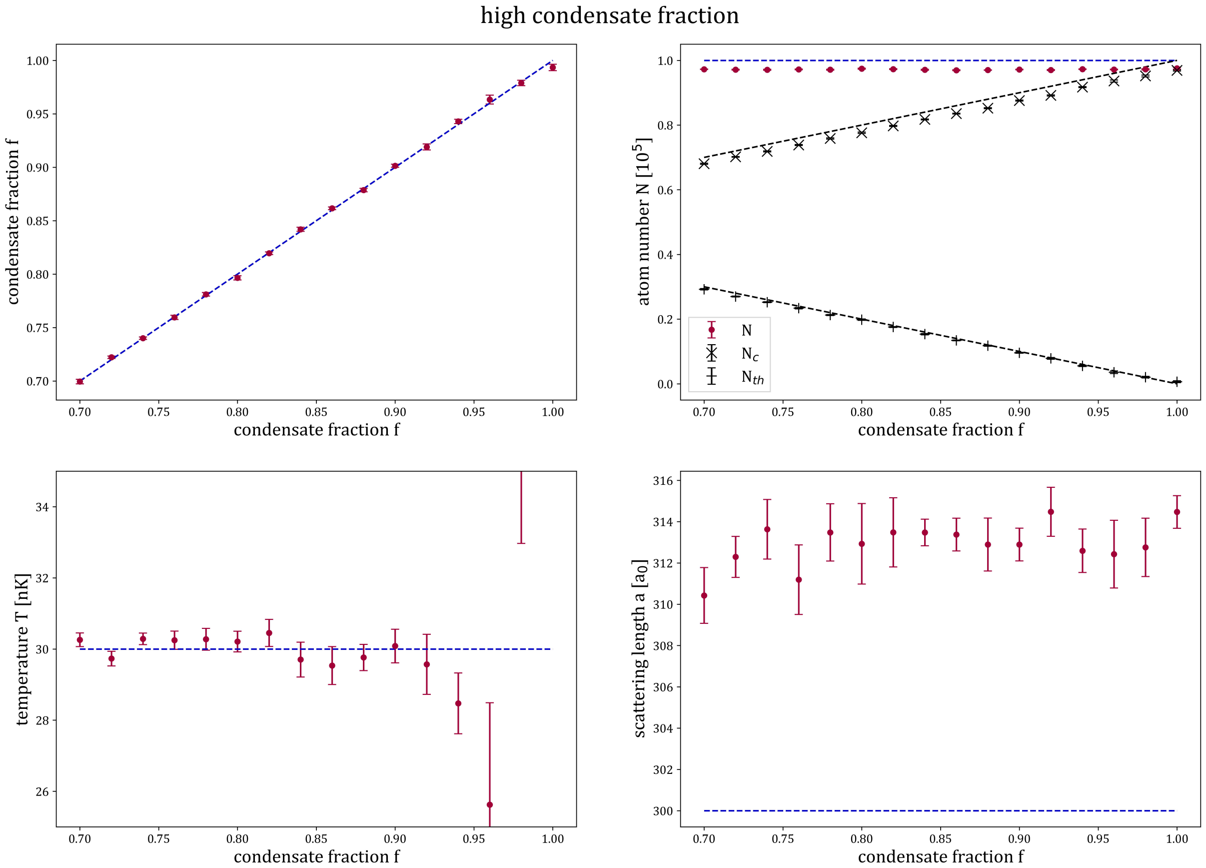

Figure 4.5: (red) mean values for condensate fraction (top left), total atom number (top right), temperature (bottom left) and scattering length (bottom right) obtained by applying the fit routine used in the experiment to 10 simulations for each condensate fraction from 70 to 100 % (bottom); (blue) expected values as fed into the simulations for trapping frequencies $\omega_{x,y,z} = 2\pi \cdot (45, 10, 126)$ Hz and a time of flight $t_{\text{tof}} = 20$ ms

In the following we investigate the situation for different time of flight durations between 12 and 38 ms, once for a low condensate fraction of 2 % and once for a high condensate fraction of 90 %. First, we look at the low condensate fraction of 2 %. The result is presented in figure 4.6. The fitted condensate fraction tends to be slightly too small but never falls below 1 %. The total atom number is again constantly underestimated to the same degree as observed before. The fitted temperatures scatter around the real value of 300 nK by up to about 3 nK. The scattering length shows relative high deviations from the real values being mostly overestimated as observed before. In general, there is no tendency of a difference in the fits reliability connected to the duration of the time of flight.

Also in the case of a high condensate fractions, there is no correlation between the duration of the time of flight and the precision of the fit as can be seen in figure 4.7. As observed before, the input condensate fraction of 90 % is determined very precisely. The same slight underestimate of N_c as before is observed, while N_{th} is always estimated well. When it comes to temperature, T is determined rather accurately with deviations of less than 1 nK. As observed before, the scattering length is slightly overestimated for high condensate fractions.

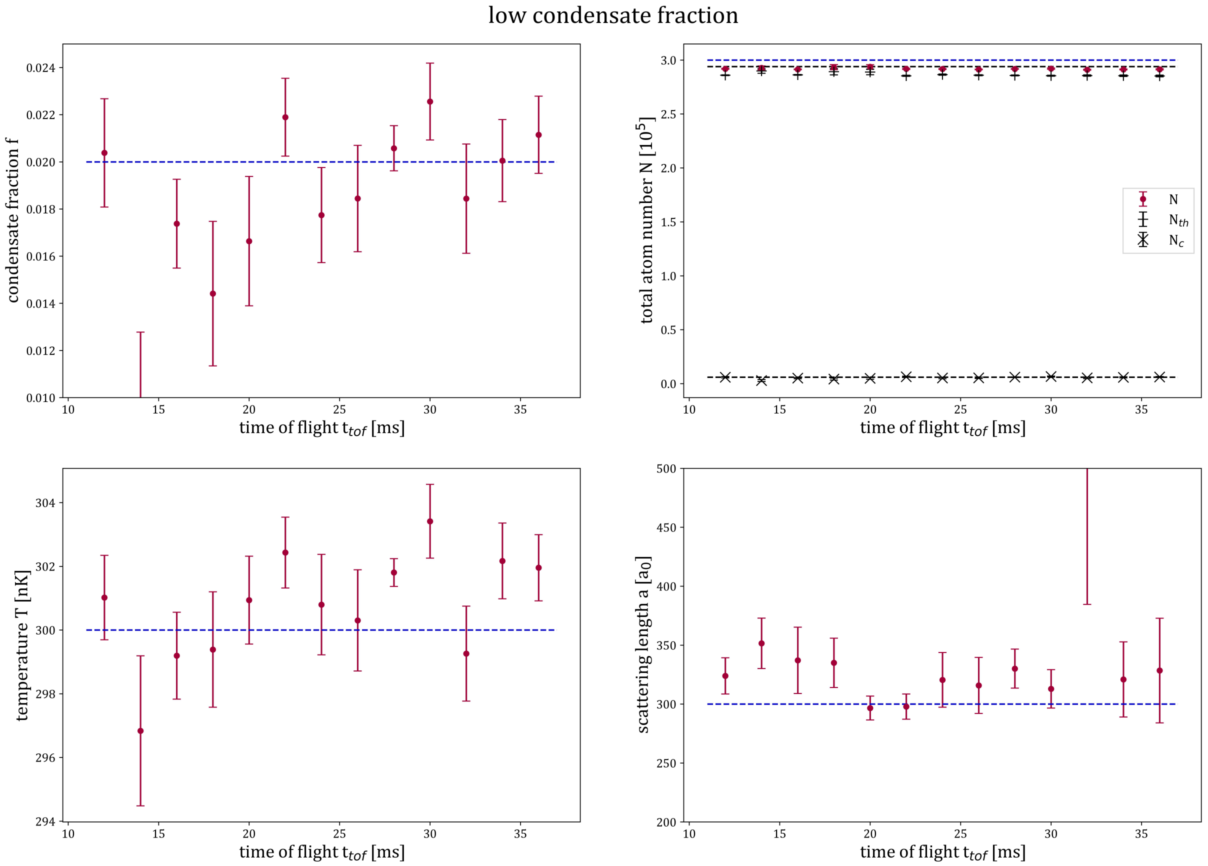

Figure 4.6: (red) mean values for condensate fraction (top left), total atom number (top right), temperature (bottom left) and scattering length (bottom right) obtained by applying the fit routine used in the experiment to 10 simulations for each time of flight from 12 to 25 ms for a condensate fraction of 2% and trapping frequencies $\omega_{x,y,z} = 2\pi \cdot (206, 96, 227)$ Hz; (blue) expected values as fed into the simulations

We briefly summarize what we found in this section. The atom number in the larger part of the atomic cloud tends to be slightly underestimated. However, it does not effect the determination of the condensate fraction in a significant way. Only the cases of a pure BEC and a pure thermal cloud are not detected as such. In general, the temperature is always determined relatively precisely with deviations of only a few nK except for very high condensate fractions. However, the estimate of the scattering length is rather imprecise especially for low condensate fractions. Slight deviations in fitting the condensate can result in high deviations of a. The overestimate of a for high condensate fractions corresponds to the underestimate of the atom number in the condensate. Furthermore, we could observe that the duration of the time of flight has no impact on the accuracy of the fit result.

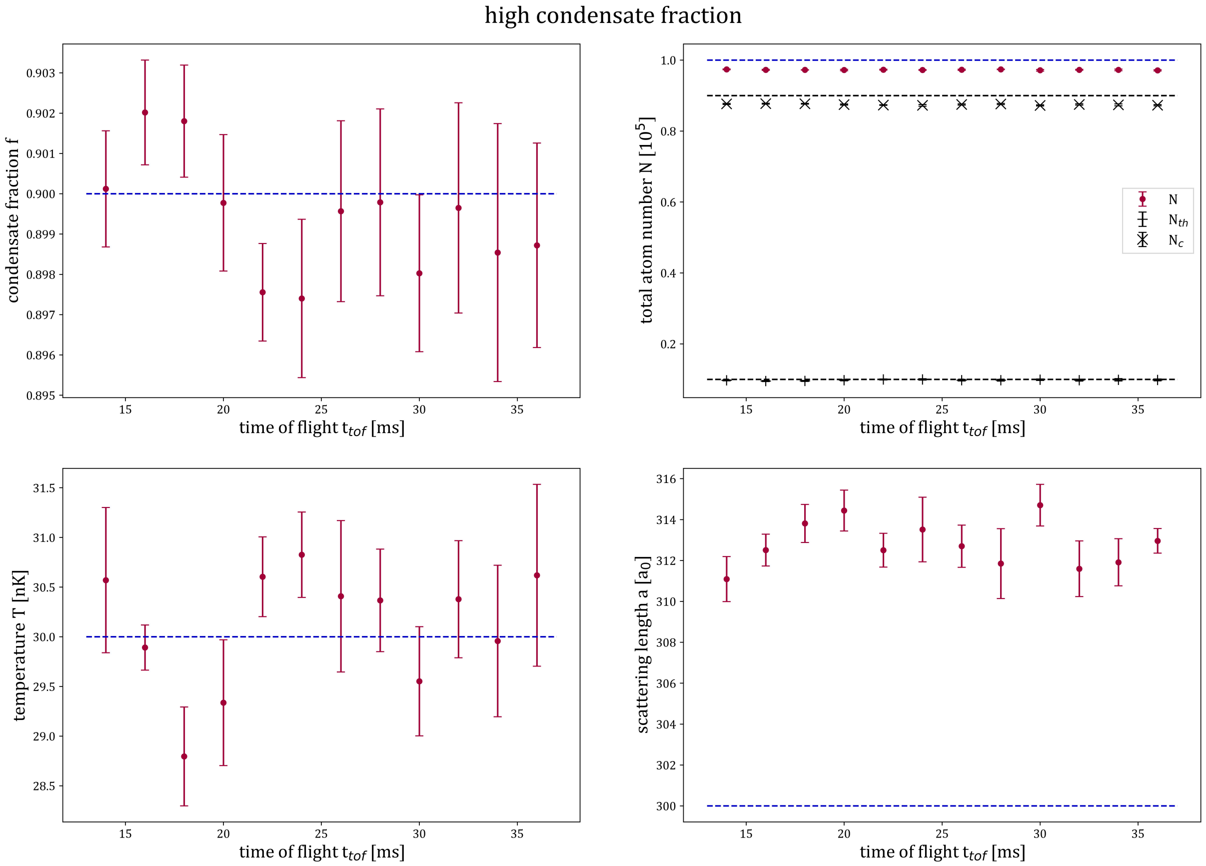

Figure 4.7: (red) mean values for condensate fraction (top left), total atom number (top right), temperature (bottom left) and scattering length (bottom right) obtained by applying the fit routine used in the experiment to 10 simulations for each time of flight from 14 to 27 ms for a condensate fraction of 90% and trapping frequencies $\omega_{x,y,z} = 2\pi \cdot (206, 96, 227)$ Hz; (blue) expected values as fed into the simulations

Chapter 5

Conclusion

In the course of this thesis an optical set-up for the conduction of absorption imaging of an ultracold Dy cloud was designed. Furthermore, the contributions to the noise that comes with the imaging was analysed and the reliability of the fitting routine that is applied to the OD images investigated.

When it comes to the optical set-up there are two major constraints to the shape of the imaging beam provided by the experimental apparatus. The laser beam must have a small enough waist to avoid any cut-off by the DPS and still be large enough to image the whole atomic cloud at different stages of the cooling process with an appropriate intensity. This was fulfilled by a telescope set-up made out of three lenses, which are placed in front of viewport CF63. That the shape of the beam meets the expectations was confirmed in a test set-up. Here also the effects of lens displacement were investigated. We found out that the last lens is suited to change the beam's shape significantly and influence position and size of the minimal waist equally. The first lens mainly influences the degree of divergence, while the last lens is suited for fine-tuning the set-up. The imaging beam is superimposed with the push beam by a PBS. We measured a degree of polarization of 99.5 %, which is a satisfying result. For projecting the atomic cloud onto the plane of the camera, we used two different imaging lenses, which create a magnification of 2 and 0.5 respectively. This allows time of flights up to 19 ms and 38 ms before the atoms fall out of the frame due to gravity.

In the second part of this thesis, we examined the contribution of different types of noise to the images, which are recorded with a CMOS camera. On the images without any incident light the only noise contribution is due to read noise, which mainly occurs statistically random as we found out. For illuminated images taken with an imaging pulse duration of 25 μs, which is used in the experiment, the relevant noise contributions are PSN and FPN. The vast majority of the FPN is due to a non-uniform illumination of the sensor. By applying the method of flatfielding it could be reduced significantly. Even though it did not become negligibly small, it was surpassed by PSN as the dominant noise source. The latter presents an intrinsic limitation to imaging.

In the last part, the observations made so far were implemented in a simulation that imitates the imaging process of absorption imaging. The simulation was adapted to the situation in the experiment by implementing a density distribution that describes the distribution of bosonic atoms at low temperatures in terms of experimentally accessible quantities. Furthermore, we fed in the characteristics of the noise that we determined before. To the obtained simulated OD images the fit routine that is also implemented in the experiment was applied. For the two situations we are interested in, namely condensate fractions close to transition and almost pure BEC, we found that the condensate fraction is always determined rather precisely. Only the absence of any condensate or thermal cloud could not be detected as such. The atom number in the larger part was slightly underestimated, what resulted in a slight underestimate of the total atom number of about 3 %. The determined temperature normally deviated from the input values by only a few Nanokelvin, except for very high condensate fractions above more than 90 %. Since the scattering length is determined from the condensate its estimation was rather imprecise for low condensate fractions. For high condensate fractions, it was much more accurate, but tended to be slightly overestimated to the degree of the underestimate of the number of atoms in the condensate. Finally, we observed that the duration of the time of flight does not influence the reliability of the fit.

In the future, further effort could be done on improving the image quality and the reliability of the fit. There are two things that have to be kept in mind when it comes to the fit routine. First, how to account for the slight underestimate of the atom number in the larger part of the atomic cloud and its effects on the other quantities and second, how to deal with pure thermal clouds or pure BECs. One approach to enhance the reliability of the fit may be improving the quality of the images. In particular, the occurrence of FPN can be decreased in two ways. On the one hand, one can minimize the influence of non-uniform illumination of the camera sensor, especially the occurrence of interference patterns. This might be achieved by using optical components of higher quality and performing a more precise alignment. On the other hand, the obtained images could undergo some sort of post-processing. Concerning the latter, the technique of flatfielding has shown a first promising result. The method could be further improved and, if appropriate, implemented in the imaging routine. With this, a good foundation is laid for the observation of further quantum mechanical phenomena in ultracold Dy gases with this experiment. In particular, the group plans to investigate thermal effects on many-body phases and the shift of the critical temperature of the BEC phase transition due to dipole-dipole interactions in the near future.

Appendix A

A.1 Acronyms

2D MOT two dimensional magneto-optical trap.

3D MOT three dimensional magneto-optical trap.

ADC analog-to-digital converter.

BEC Bose-Einstein condensate.

CCD charge-coupled device.

CDS correlated double sampling circuit.

CMOS complementary metal oxide semiconductor.

DPS differential pumping stage.

Dy Dysprosium.

FPN fixed pattern noise.

MOT magneto-optical trap.

OD optical density.

ODT optical dipole trap.

PBS polarizing beam splitter.

PRNU photo response non-uniformity.

PSN photon shot noise.

PTC photon transfer curve.

QE quantum efficiency.

A.2 Program for Simulating the Optical Set-Up

```
## imports
import numpy as np
import pandas as pd

## properties of the collimated beam
lam = 421e-6     # wavelenght in mm
w0 = 1.022       # waist of the collimated beam
n = 1            # refractive index

## helpful functions
# Rayleigh range
def x_R (w_min):
    return np.pi * w_min**2 * n/lam
# waist along the x-axis depending on the size and position of the
# minimal waist
def w (x, w_min, x_min):
    return w_min*np.sqrt(1+((x-x_min)/x_R(w_min))**2)
# waist after focusing a collimated beam
def focusing (f, w_in):
    w_fin = np.abs(lam*f/np.pi/w_in)
    x_fin = f
    return w_fin, x_fin
# change of the beam waist due to a thin lens
def lens (f, w_in, x_in):
    M_r = np.abs(f/(x_in-f))
    r = x_R(w_in)/(x_in-f)
    M = M_r/np.sqrt(1+r**2)
    w_fin = M*w_in
    x_fin = M**2*(x_in - f)+f
    return w_fin, x_fin

## finding an appropriate set-up
# possible lenses to choose from
f1_in = np.array([-100, -60, 60, 100, 125, 150, 175, 200, 300, 400])
f2_in = np.array([40, 100, 250, 300, 500, 750])
f3_in = np.array([40, 100, 250, 300, 500, 750])

# distance of the lenses
l1_in = np.arange([0, 1200, 5])
l2_in = np.arange([0, 1200, 5])
l3_in = np.arange([0, 1200, 5])
```

```
# empty arrays to store the calculated values
f1 = np.ones(len(f1_in)*len(f2_in)*len(f3_in)*len(l1_in)*len(l2_in)*
        len(l3_in))
f2 = np.ones(len(f1_in)*len(f2_in)*len(f3_in)*len(l1_in)*len(l2_in)*
        len(l3_in))
f3 = np.ones(len(f1_in)*len(f2_in)*len(f3_in)*len(l1_in)*len(l2_in)*
        len(l3_in))
d12 = np.ones(len(f1_in)*len(f2_in)*len(f3_in)*len(l1_in)*len(l2_in)*
        len(l3_in))
d23 = np.ones(len(f1_in)*len(f2_in)*len(f3_in)*len(l1_in)*len(l2_in)*
        len(l3_in))
w1 = np.ones(len(f1_in)*len(f2_in)*len(f3_in)*len(l1_in)*len(l2_in)*
        len(l3_in))
w2 = np.ones(len(f1_in)*len(f2_in)*len(f3_in)*len(l1_in)*len(l2_in)*
        len(l3_in))
w3 = np.ones(len(f1_in)*len(f2_in)*len(f3_in)*len(l1_in)*len(l2_in)*
        len(l3_in))
x1 = np.ones(len(f1_in)*len(f2_in)*len(f3_in)*len(l1_in)*len(l2_in)*
        len(l3_in))
x2 = np.ones(len(f1_in)*len(f2_in)*len(f3_in)*len(l1_in)*len(l2_in)*
        len(l3_in))
x3 = np.ones(len(f1_in)*len(f2_in)*len(f3_in)*len(l1_in)*len(l2_in)*
        len(l3_in))
xR1 = np.ones(len(f1_in)*len(f2_in)*len(f3_in)*len(l1_in)*len(l2_in)*
        len(l3_in))
xR2 = np.ones(len(f1_in)*len(f2_in)*len(f3_in)*len(l1_in)*len(l2_in)*
        len(l3_in))
xR3 = np.ones(len(f1_in)*len(f2_in)*len(f3_in)*len(l1_in)*len(l2_in)*
        len(l3_in))
l1 = np.ones(len(f1_in)*len(f2_in)*len(f3_in)*len(l1_in)*len(l2_in)*
        len(l3_in))
l2 = np.ones(len(f1_in)*len(f2_in)*len(f3_in)*len(l1_in)*len(l2_in)*
        len(l3_in))
l3 = np.ones(len(f1_in)*len(f2_in)*len(f3_in)*len(l1_in)*len(l2_in)*
        len(l3_in))
w_lens2 = np.ones(len(f1_in)*len(f2_in)*len(f3_in)*len(l1_in)*
        len(l2_in)*len(l3_in))
w_lens3 = np.ones(len(f1_in)*len(f2_in)*len(f3_in)*len(l1_in)*
        len(l2_in)*len(l3_in))
w_CF63 = np.ones(len(f1_in)*len(f2_in)*len(f3_in)*len(l1_in)*
        len(l2_in)*len(l3_in))
```

```
w_DPSbeg = np.ones(len(f1_in)*len(f2_in)*len(f3_in)*len(l1_in)*
        len(l2_in)*len(l3_in))
w_DPSend = np.ones(len(f1_in)*len(f2_in)*len(f3_in)*len(l1_in)*
        len(l2_in)*len(l3_in))
w_BEC = np.ones(len(f1_in)*len(f2_in)*len(f3_in)*len(l1_in)*
        len(l2_in)*len(l3_in))
w_CF40 = np.ones(len(f1_in)*len(f2_in)*len(f3_in)*len(l1_in)*
        len(l2_in)*len(l3_in))
w_camera = np.ones(len(f1_in)*len(f2_in)*len(f3_in)*len(l1_in)*
        len(l2_in)*len(l3_in))
r_lens2 = np.ones(len(f1_in)*len(f2_in)*len(f3_in)*len(l1_in)*
        len(l2_in)*len(l3_in))
r_lens3 = np.ones(len(f1_in)*len(f2_in)*len(f3_in)*len(l1_in)*
        len(l2_in)*len(l3_in))
r_PBS = np.ones(len(f1_in)*len(f2_in)*len(f3_in)*len(l1_in)*
        len(l2_in)*len(l3_in))
r_CF63 = np.ones(len(f1_in)*len(f2_in)*len(f3_in)*len(l1_in)*
        len(l2_in)*len(l3_in))
r_DPSbeg = np.ones(len(f1_in)*len(f2_in)*len(f3_in)*len(l1_in)*
        len(l2_in)*len(l3_in))
r_DPSend = np.ones(len(f1_in)*len(f2_in)*len(f3_in)*len(l1_in)*
        len(l2_in)*len(l3_in))
r_BEC = np.ones(len(f1_in)*len(f2_in)*len(f3_in)*len(l1_in)*
        len(l2_in)*len(l3_in))
r_CF40 = np.ones(len(f1_in)*len(f2_in)*len(f3_in)*len(l1_in)*
        len(l2_in)*len(l3_in))
r_camera = np.ones(len(f1_in)*len(f2_in)*len(f3_in)*len(l1_in)*
        len(l2_in)*len(l3_in))
I_BEC = np.ones(len(f1_in)*len(f2_in)*len(f3_in)*len(l1_in)*
        len(l2_in)*len(l3_in))
I_effCameraSize = np.ones(len(f1_in)*len(f2_in)*len(f3_in)*
        len(l1_in)*len(l2_in)*len(l3_in))

# calculate the data in a loop
counter = 0
for i in range (len(f1_in)):
    for j in range (len(f2_in)):
        for k in range (len(f3_in)):
            for l in range (len(l1_in)):
                for m in range (len(l2_in)):
                    for o in range (len(l3_in)):
                        # input parameters (focal lenghts, distances)
```

```
f1[counter] = f1_in[i]
f2[counter] = f2_in[j]
f3[counter] = f3_in[k]
# distance of the lenses from CF63
l1[counter] = l1_in[l]
l2[counter] = l2_in[m]
l3[counter] = l3_in[o]
d12[counter] = l1[counter] - l2[counter]
d23[counter] = l2[counter] - l3[counter]
# size and position of the minimal waist
w1[counter], x1[counter] = focusing(
                            f1[counter], w0)
xR1[counter] = x_R(w1[counter])
w2[counter], x2[counter] = lens(f2[counter],
                    w1[counter],
                    d12[counter]-x1[counter])
xR2[counter] = x_R(w2[counter])
w3[counter], x3[counter] = lens(f3[counter],
                    w2[counter],
                    d23[counter]-x2[counter])
xR3[counter] = x_R(w3[counter])
# size of the beam waist at different positions
w_lens2[counter] = w(d12[counter], w1[counter],
                    x1[counter])
w_lens3[counter] = w(d23[counter], w2[counter],
                    x2[counter])
w_CF63[counter] = w(0, w3[counter],
                    x3[counter]-l3[counter])
w_DPSbeg[counter] = w(206, w3[counter],
                    x3[counter]-l3[counter])
w_DPSend[counter] = w(261.7, w3[counter],
                    x3[counter]-l3[counter])
w_BEC[counter] = w(534, w3[counter],
                    x3[counter]-l3[counter])
w_CF40[counter] = w(534+101, w3[counter],
                    x3[counter]-l3[counter])
w_camera[counter] = w(534+101+349, w3[counter],
                    x3[counter]-l3[counter])
# radii of the beam at different positions
r_lens2[counter] = 3*w_lens2[counter]
theta = np.arctan(r_lens2[counter]/x2[counter])
if r_lens2[counter] > 25.4:
```

```
    r_lens2[counter] = 25.4
    theta = np.arctan(25.4/x2[counter])
r_lens3[counter] = np.abs(np.tan(theta)*
                    (d23[counter]-x2[counter]))
theta = np.arctan(r_lens3[counter]/x3[counter])
if r_lens3[counter] > 25.4:
    r_lens3[counter] = 25.4
    theta = np.arctan(25.4/
                    (d23[counter]-x2[counter]))
r_PBS[counter] = np.tan(theta)*(x3[counter]-
                l3[counter]+85+25.4/2)
r_CF63[counter] = np.tan(theta)*
                (x3[counter]-l3[counter])
r_DPSbeg[counter] = np.tan(theta)*np.abs(
                (x3[counter]-l3[counter]-206))
if r_DPSbeg[counter] > 1:
    r_DPSbeg[counter] = 1
    theta = np.arctan(1/
            np.abs(x3[counter]-l3[counter]-206))
r_DPSend[counter] = np.tan(theta)*np.abs(
                    (x3[counter]-l3[counter]-
                    261.7))
if r_DPSend[counter] > 2.9:
    r_DPSend[counter] = 2.9
    theta = np.arctan(2.9/
            np.abs((x3[counter]-l3[counter]-
            261.7)))
r_BEC[counter] = np.tan(theta)*
                (534+l3[counter]-x3[counter])
r_CF40[counter] = np.tan(theta)*(534+101+
                l3[counter]-x3[counter])
r_camera[counter] = np.tan(theta)*
                (534+101+349+
                l3[counter]-x3[counter])
# intensity of the beam at the radius compared
# to the center in the plane of the BEC
I_BEC[counter] = np.exp(-2*r_BEC[counter]**2/
                w_BEC[counter]**2)
I_effCameraSize[counter] = np.exp(-2*11.25**2/
                            w_BEC[counter]**2)
# repetitions
counter = counter + 1
```

```
# create a pandas dataFrame
result = pd.DataFrame(
    {
      "f1": f1,
      "f2": f2,
      "f3": f3,
      "d12": d12,
      "d23": d23,
      "l1": l1,
      "l2": l2,
      "l3": l3,
      "w1": w1,
      "w2": w2,
      "w3": w3,
      "x1": x1,
      "x2": x2,
      "x3": x3,
      "xR1": xR1,
      "xR2": xR2,
      "xR3": xR3,
      "w_lens2": w_lens2,
      "r_lens2": r_lens2,
      "w_lens3": w_lens3,
      "r_lens3": r_lens3,
      "r_PBS": r_PBS,
      "w_CF63": w_CF63,
      "r_CF63": r_CF63,
      "w_DPS_beg": w_DPSbeg,
      "r_DPS_beg": r_DPSbeg,
      "w_DPS_end": w_DPSend,
      "r_DPS_end": r_DPSend,
      "w_BEC": w_BEC,
      "r_BEC": r_BEC,
      "w_CF40": w_CF40,
      "r_CF40": r_CF40,
      "w_camera": w_camera,
      "r_camera": r_camera,
      "I/I0_BEC": I_BEC,
      "I/I0_effCamera": I_effCameraSize
    }
)
```

A.3 Implementation of the Density Distribution of a Bosonic Cloud

```
# imports
import numpy as np
import scipy.constants as const
import scipy.integrate as integrate

# polylog function
Li2_vec = np.vectorize(lambda x:
        np.array(mp.fp.polylog(2, x), dtype=np.complex128))

# density distsribution
def n2D_bose(xy_mesh, T, N, f, omgx, omgy, omgz, a_fac, tof):
    """
    calculate the column density distribution for partly condensed cloud
    of bosons

    Parameters
    ----------
    x, y:   arrays(float)
            observed area in the x,y-plane
    T:      float
            temperture of the condensate [K]
    N:      float
            total atom number
    f:      float
            condensate fraction
    omgx, omgy, omgz: floats
            trapping frequencies in x,y,z direction [1/s]
    a_fac:  float
            scattering lenght in terms of the Bohr radius [a_0]
    tof:    time of flight
            duration of the time of flight [s]

    Returns
    -------
    n2Dtot: 2DArray(float)
            array whith column density for each point in the
            x,y-plane [1/m^2]
    """
```

```
x, y = xy_mesh
m = 164*const.u
Nc = f*N
omg = (omgx*omgy*omgz)**(1/3)
aho = np.sqrt(const.hbar/(m*omg))
ahox = np.sqrt(const.hbar/(m*omgx))
ahoy = np.sqrt(const.hbar/(m*omgy))
ahoz = np.sqrt(const.hbar/(m*omgz))
a = a_fac * 4*np.pi*const.epsilon_0*const.hbar**2/
    (const.e**2*const.electron_mass)
mu = const.hbar*omg/2*(15*Nc*a/aho)**(2/5)
g = 4*const.pi*const.hbar**2*a/m
Rxth = np.sqrt(const.k*T/m*(1/omg**2+tof**2))
Ryth = np.sqrt(const.k*T/m*(1/omg**2+tof**2))
Rxc = np.sqrt(const.hbar*omgx/m)*np.sqrt(
        (1+omgx**2*tof**2)/omgx**2)*(15*Nc*a/ahox)**(1/5)
Ryc = np.sqrt(const.hbar*omgy/m)*np.sqrt(
        (1+omgy**2*tof**2)/omgy**2)*(15*Nc*a/ahoy)**(1/5)
Rzc = np.sqrt(const.hbar*omgz/m)*np.sqrt(
        (1+omgz**2*tof**2)/omgz**2)*(15*Nc*a/ahoz)**(1/5)
n2D0c = 4/3*Rzc*mu/g*1/(1+omgx**2*tof**2)**(1/2)*1/
        (1+omgy**2*tof**2)**(1/2)*1/(1+omgz**2*tof**2)**(1/2)
if (Rxth == 0) or (Ryth == 0):
    n2D0th = 0
    n2Dth = 0
else:
    n2D0th = (1-f)*N*integrate.nquad(
            lambda x,y:
            np.real(Li2_vec(np.exp(-(x/Rxth)**2-(y/Ryth)**2))),
            [[-6/np.sqrt(2)*Rxth, 6/np.sqrt(2)*Rxth],
            [-6/np.sqrt(2)*Ryth, 6/np.sqrt(2)*Ryth]])[0]**(-1)
    n2Dth = n2D0th * np.real(Li2_vec(np.exp(-(x/Rxth)**2-(y/Ryth)**2)))
argument = 1-(x/Rxc)**2-(y/Ryc)**2
n2Dc =  n2D0c * np.piecewise(argument, [argument<=0, argument>0],
        [0, lambda argument: argument])**(3/2)
n2Dtot = n2Dc + n2Dth
return n2Dtot
```

B Bibliography

[1] Felix Borchers. Modelling of absorption imaging of degenerate fermi gases in ultracold atom experiments, 2023.

[2] Yuan Chen, S.M. Guertin, M. Petkov, D.N. Nguyen, and F. Novak. A chip and pixel qualification methodology on imaging sensors. In *2004 IEEE International Reliability Physics Symposium. Proceedings*, pages 435–439, 2004.

[3] Franco Dalfovo, Stefano Giorgini, Lev P. Pitaevskii, and Sandro Stringari. Theory of bose-einstein condensation in trapped gases. *Reviews of Modern Physics*, 71(3):463–512, apr 1999.

[4] W. Demtröder. *Experimentalphysik 3: Atome, Moleküle und Festkörper*. Springer-Lehrbuch. Springer Berlin Heidelberg, 2016.

[5] Melina Filzinger. Improved manipulation and detection of an ultracold 6li-133cs mixture towards the investigation of the bose polaron, 2018.

[6] Jianshun Gao. A first two-dimensional magneto-optical trap for dysprosium, 2022.

[7] Christian Gölzhäuser. Building a new dy quantum gas experiment, 2021.

[8] J.R. Janesick and American Institute of Physics. *Photon Transfer: DN [lambda]*. SPIE, 2007.

[9] Shuwei Jin, Jianshun Gao, Karthik Chandrashekara, Christian Gölzhäuser, Joschka Schöner, and Lauriane Chomaz. Two-dimensional magneto-optical trap of dysprosium atoms as a compact source for efficient loading of a narrow-line three-dimensional magneto-optical trap. *Phys. Rev. A*, 108:023719, Aug 2023.

[10] W. Ketterle, D. S. Durfee, and D. M. Stamper-Kurn. Making, probing and understanding bose-einstein condensates, 1999.

[11] Hanamatsu Photonics K.K. *Digital CMOS Camera C11440-36U Instruction Manual*, 2016.

[12] Mikhail Konnik and James Welsh. High-level numerical simulations of noise in ccd and cmos photosensors: review and tutorial. *arXiv preprint arXiv:1412.4031*, 2014.

[13] Inc. MKS Instruments. *LBP2 Laser Beam Prfiler*, 2021.

[14] Bahaa EA Saleh and Malvin Carl Teich. *Fundamentals of photonics*. john Wiley & sons, 2019.

[15] Matthias Scholl. *Probing an ytterbium Bose-Einstein condensate using an ultranarrow optical line: Towards artificial gauge fields in optical lattices*. PhD thesis, UPMC Université Paris VI, 2014.

[16] Joschka Schöner. Magnetic-field setup for magneto-optical-trapping and interaction-tuning in novel dysprosium quantum gas experiment, 2022.

[17] Daniel A Steck. Quantum and atom optics. 2007.

Acknowledgment

I want to use this last page to express my gratitude to some people who have supported me a lot during the creation of this thesis as well as during the last couple of years.

First and foremost, I want to express my deepest gratitude to Lauriane Chomaz for her close mentorship. Thanks for all the advice, explanations and the opportunity to contribute to the creation of a new experiment. I have learned a lot during the last few months and I am grateful that you gave me this opportunity.

Furthermore, I want to thank the whole Quantum Fluids group, namely Shuwei Jin, Wyatt Kirkby, Jianshun Gao, Karthik Chandrashekara, Sara Philips, Charles Drevon, Thibault Bourgeois, Christian Gölzhäuser, Joschka Schöner and Maurice Rieger. Thanks for welcoming me among you, for nice lunch breaks and fun evening activities.

Among the others I owe particular thanks to Jianshun Gao for his time and patience in answering all my questions on code and optics.

Special thanks also go to Christian Enss for kindly being my second examiner.

Besides that, I want to thank my friends for going through not always easy times at university together, including some semesters under the influence of the COVID pandemic. You made studying much more enjoyable and probably I was not at this point without you.

Last but not least, I want to thank my parents for their invaluable support: mentally, financially and in any other way possible. You are always there for me and encourage all the decisions I make. Thank You!

Erklärung

Ich versichere, dass ich diese Arbeit selbstständig verfasst und keine anderen als die angegebenen Quellen und Hilfsmittel benutzt habe.

Heidelberg, den 10. September 2023,

B. Ba

Britta Bader